METHOD DEVELOPMENT IN THE NEGF FRAMEWORK: MAXIMALLY LOCALIZED WANNIER FUNCTION AND BÜTTIKER PROBE FOR MULTI-PARTICLE INTERACTION

A Dissertation

Submitted to the Faculty

of

Purdue University

by

Kuang-Chung Wang

In Partial Fulfillment of the

Requirements for the Degree

of

Doctor of Philosophy

December 2019

Purdue University

West Lafayette, Indiana

THE PURDUE UNIVERSITY GRADUATE SCHOOL
STATEMENT OF DISSERTATION APPROVAL

Dr. Tillmann Kubis, co-Chair

School of Electrical and Computer Engineering

Dr. Gerhard Klimeck, co-Chair

School of Electrical and Computer Engineering

Dr. Supriyo Datta

School of Electrical and Computer Engineering

Dr. Alejandro Strachan

School of Material Science Engineering

Approved by:

Dr. Dimitrios Peroulis

Head of the School Graduate Program

I express my sincere gratitude to my family, my friends, my advisors and all who have supported me differently on this journey.

ACKNOWLEDGMENTS

I would like to thank my committee co-chair and co-advisor Professor Tillmann Kubis for meeting with me weekly. He spent time learning the issues, provided guidance and was always critical with my results. Crash course on NEGF was voluntarily offered despite his busy schedule to broaden engineering students' perspective from a physicist's viewpoint. I also am grateful for him spending months on each paper with me that I learned how to write a scientific document that is reproducible and covering details I couldn't have possibly imagined. I want to thank my other co-chair and co-advisor, Professor Gerhard Klimeck, as a visioner founded this lab, umbrellaed us under the resourceful entity NCN with abundant computational/financial resources and embraced me into this exciting opportunity. He provided me invaluable advice on this journey especially had long lasting impact developing our most important skill in this world and lifetime - presentation skill. He indoctrinated us the importance of being concise and effective with scientific communication. Furthermore, he is exemplary in simplifying and elucidating complicated physics and phenomena with his words. Furthermore, financial support for the tuition, stipend and conference traveling were provided by both of them and kept students focusing on academic achievements. Last but not the least, they also helped me explore and analyze my future career possibilities. I am and should be forever grateful for their endeavors.

Thanks for my committee members Prof. Supriyo Datta and Prof. Alejandro Strachan to make time for my Ph.D. exams and also have been helpful and flexible for timely discussions. They have offered DFT and NEGF courses that elevated and laid us the foundation for the real world research ahead of us.

Thanks for my friends and colleagues Chin-Yi Chen, Camilo Duarte, Daniel Valencia, Prasad Sarangapani, James Charles, Hesameddin Ilatikhameneh, Tarek Ameen, Yuanchen Chu, Xinchen Guo, Yaohua Tan, Yu He, Michael Povolotskyi, Jun Huang,

TABLE OF CONTENTS

LIST OF TABLES

LIST OF FIGURES

Figure   Page

ABSTRACT

Wang, Kuang-Chung Ph.D., Purdue University, December 2019. Method Development in the NEGF Framework: Maximally Localized Wannier Function and Büttiker Probe for Multi-particle Interaction. Major Professor: Prof. Gerhard KLIMECK Prof. Tillmann KUBIS.

The work involves two new method implementation and application in the Quantum transport community for nano-scale electronic devices.

First method: Ab-initio Tight-Binding(TB)

As the surfacing of novel 2D materials, layers can be stacked freely on top of each other bound by Van der Waals force with atomic precision. New devices created with unique characteristics will need the theoretical guidance. The empirical tight-binding method is known to have difficulty accurately representing Hamiltonian of the 2D materials. Maximally localized Wannier function(MLWF) constructed directly from ab-initio calculation is an efficient and accurate method for basis construction. Together with NEGF, device calculation can be conducted. The implementation of MLWF in NEMO5 and the application on 2D MOS structure to demystify interlayer coupling are addressed.

Second method: Büttiker-probe Recombination/Generation(RG) method:

The non-equilibrium Green function (NEGF) method is capable of nanodevice performance predictions including coherent and incoherent effects. To treat incoherent scattering, carrier generation and recombination is computationally very expensive. In this work, the numerically efficient Büttiker-probe model is expanded to cover recombination and generation effects in addition to various incoherent scattering processes. The capability of the new method to predict nanodevices is exemplified with quantum well III-N light-emitting diodes and photo-detector. Comparison is made

with the state of art drift-diffusion method. Agreements are found to justify the method and disagreements are identified attributing to quantum effects.

The two menthod are individually developed and utilized together to study BP/MoS_2 interface. In this vertical 2D device, anti-ambipolar(AAP) IV curve has been identified experimentally with different explanation in the current literature. An atomistic simulation is performed with basis generated from density functional theory. Recombination process is included and is able to explain the experiment findings and to provide insights into 2D interface devices.

1. INTRODUCTION

1.1 Motivation

Non-equilibrium Green's function has been proven necessary for nano-scale electronic devices study. It allows us to optimize nano-device with quantum mechanics using open boundary condition under non-equilibrium condition, in other words, with voltage difference across the device. Two main applications of devices are pursued in this work and explained individually in the following sections. Both of them are devices based on pn junctions, however, different in materials, device architecture, and the involved multi-particles interaction mechanisms. With two new methods implemented in NEMO5, we are able to address the difficulties of simulating such devices.

1.1.1 Optoelectronics, the last mile of efficiency boost

With lighting consuming 15 % of the electricity consumption [1], solid state lighting as one of the highest efficiency light source can reduce the number to 4%. It can therefore save around \$150B/year of energy and infrastructure and reduce the carbon emission by 200M tons/year [2].

The success of GaN with LEDs [2] arises from the material nature with direct band gap of 3.45 eV, corresponding to near-ultraviolet light. In combination with other nitrides forming alloy, the band gap has a wide range. Since identified in 1960s as a candidate for LED, material quality has been improved, doping technique has been discovered, therefore, efficiency has been increased. However, mystery remains with their conflicting high density of dislocations and startling high efficiency (more than 10^{10} cm^{-3} [3,4]). Indium fluctuation non-uniformity of the device has been proposed

such that carrier can avoid the traps by residing in the perturbed energy landscape. With such in-homogeneity, Urbach tail can form both in the well and the barrier regions [5]. Furthermore, with defects in the GaN [6], tunneling current between the well can be assisted as shown in [7]. To address those issues, the deficiency of the existing models are shown while a new model is needed and addressed in this work.

1.1.2 2D pn junction

Since the discovery of Graphene in 2004 with high mobility and unusual physical phenomena, 2D materials has inspired new device architectures, new characteristics and new applications. The first advantage is the ability to combine different materials as atomic Lego [8]. Materials not only have their unique band structures, but also are tunable by strain, thickness, and rotations adding potential engineering dimensions.

pn junction serves as the basic building blocks for many applications, e.g. diode, LED, transistors, logic gates,etc., and has been thoroughly studied as textbook example. However with the emergence of 2D materials, materials of complete opposite characteristic can be combined. p and n types can be combined to form atomic 2D pn junctions [9] with the potential for transparent, flexible, high-efficiency electronic and optoelectronic applications.

Different device architectures have been expereimentally demonstrated. Planar 2D pn junction is shown to have a longer depletion width [10] to reduce Fermi level pinning. Vertical junction [11] is shown to demonstrate gate tunability and anti-ambipolar characteristics.

Many questions remain unknown with sprouting new materials and new geometry. The interlayer charge transfer remains controversial. Shockley Read Hall(SRH), Langevin processes have been proposed to dominate in the MoS_2-WSe_2 pn junction [9]. Band to band tunneling (BTBT) is used to explain the Esaki diode [12] in the revert bias region.

To explain the anti-ambipolar trend(AAP), what is the mechanism involved? Can we quantify each contribution? Can we help optimize the device? Those are the questions to be answered.

1.2 To achieve the goals

1.2.1 Develop new model for carrier recombination

To study the above mentioned problem, a tool with atomistic resolution is needed for these atomically thin structures. Furthermore, as the wave nature of the particles emerges with as device scale, a quantum mechanic picture is needed.

Current commercialized modeling tools APSYS by Crosslight Software [13], Silvaco TCAD [14] and SimuLED by STR group [15] utilize drift-diffusion. The equations assume carriers as particles satisfying newton equations. It is highly efficient however missing the wave nature of the carriers transport and therefore ignores quantum phenomena such as tunneling, confinement, and interference effects. Nevertheless, a spatially continuous recombination and generations profile can be incorporated satisfying the current conservation equations. The method has successfully assisted the science community to probe the unknown territory [9].

The state of art NEGF Multi-Eqneq calculation successfully included quantum mechanics in the formalism and demonstrated success in simulating commercialized device of III-V LEDs [16]. The model separately models electrons and holes in the device considering the recombination to reach current conservation. However, it succumbs to the limitation of having a barrier regions and assuming complete thermalizations in the well regions. With the application in mind of 2D material, with inter-facial roughness and to tackle the band-tail in barriers, a new model is needed.

In the new model proposed here, Büttiker probe will be used in a newer fashion with outgoing current into the probe mimicking carrier recombination for electron and holes. More computation power is needed however with a continuous resolution and current conservation achieved which allows us to assess novel devices performance.

1.2.2 Ab initio tight-binding transport calculation

The concept of using basis to expand the wave function helps and enables solving Schrodinger equation. Effective mass approximation (EMA) assumes materials with parabolic dispersion for carriers at the bandedge. Tight-binding method [17] assumes atomic orbitals as basis to describe the device Hamiltonian. k.p method utilize wavefunction at a certain k point to expand other k point information with Taylor expansion. It is shown that more complete basis can resemble more band structure and therefore capture the real materials more precisely, however, at the expense of higher computational cost.

All the above have drawbacks of transferability of different materials. A fitting is therefore required for targets either from experiment measured quantity or density-functional theory(DFT). For novel materials, the access of experiment may be rare. For targeting DFT band structure, the fitting process involves tens or hundreds of parameters. In this work, maximally localized Wannier function (MLWF) [18] is utilized for a direct mapping of the DFT to localized basis as tight-binding for probing device applications with novel material consideration.

2. AB-INITIO BASIS METHOD

2.1   Conventional method

2.1.1   Tight-binding method

(recapped from [19] chapter 4) To solve Schroedinger equation, the first assumption is that the solution wave function can be expanded as a set of basis $u_m(r)$ with weighting phi_m

$$\Phi(r) = \sum_m \phi_m u_m(r) \tag{2.1}$$

Substituting the solution into the Schrodinger equation $E\Phi(r) = H_{op}\Phi(r)$, we can obtain

$$E \sum_m \phi_m u_m(r) = \sum_m \phi_m H_{op} u_m(r) \tag{2.2}$$

Multiply both sides by $u_n^*(r)$ and integrate over all r we can get,

$$E \sum_m S_{nm}\phi_m = \sum_m H_{nm}\phi_m. \tag{2.3}$$

Note that S_{nm} is the overlapping integral between $u_n^*(r)$ and $u_m(r)$. H_{nm} is the integral of $u_n^*(r)H_{op}u_m(r)$

In the tight-binding method, the search for $u_m(r)$ is ignored with the goal of generating parameters [20] to construct H_{nm} directly, according to the Slater Koster table construction rule [21] with the assumption that basis are orthogonal such that S_{nm} being an identity matrix.

2.1.2 Density functional theory

The DFT starts from the following effective independent-particle Hamiltonian [22]. The first three term are kinetic energy, the electrostatic force from the nuclei, and the electrostatic force from the electron density respectively. The fourth term is an assumed existed functional that provide the exchange-correlation energy. Different methods have been proposed to approximate the term, namely, GGA, LDA, and hybrid functional..., each specialized in certain conditions.

$$\left[-\frac{1}{2}\nabla^2 - \sum_n \frac{Z_n}{|r - R_n|} + \int d^3 r' n(r') \frac{1}{|r - r'|} + V_{xc}[n](r) \right] \psi_k(r) = \epsilon \psi_k(r) \quad (2.4)$$

It has to be self-consistently solved with the electron density with N electrons in the system

$$n(r) = \sum_{k=1}^{N} |\psi_k(r)|^2. \quad (2.5)$$

In a crystal structure system, due to the symmetry and Bloch's theorem, the problem becomes a small cells with Bloch boundary conditions solved in the Brillouin zone for k point sampling. The solution is composed of a periodic function with plane waves. The advantage is for it being a complete basis, ease of implementation of energy term with fast fourier transform.

$$\psi_{nk}(r) = u_{nk} e^{ikr} \quad (2.6)$$

However, with highly localized wavefuncntion, high energy waves will be needed and worsen the computational performance. Projected augmented waves are therefore used with smoothened pseudo-potential at the core.

2.2 MLWF flowchart

The MLWF basis's interface with NEMO5 is shown in Fig. 2.1.
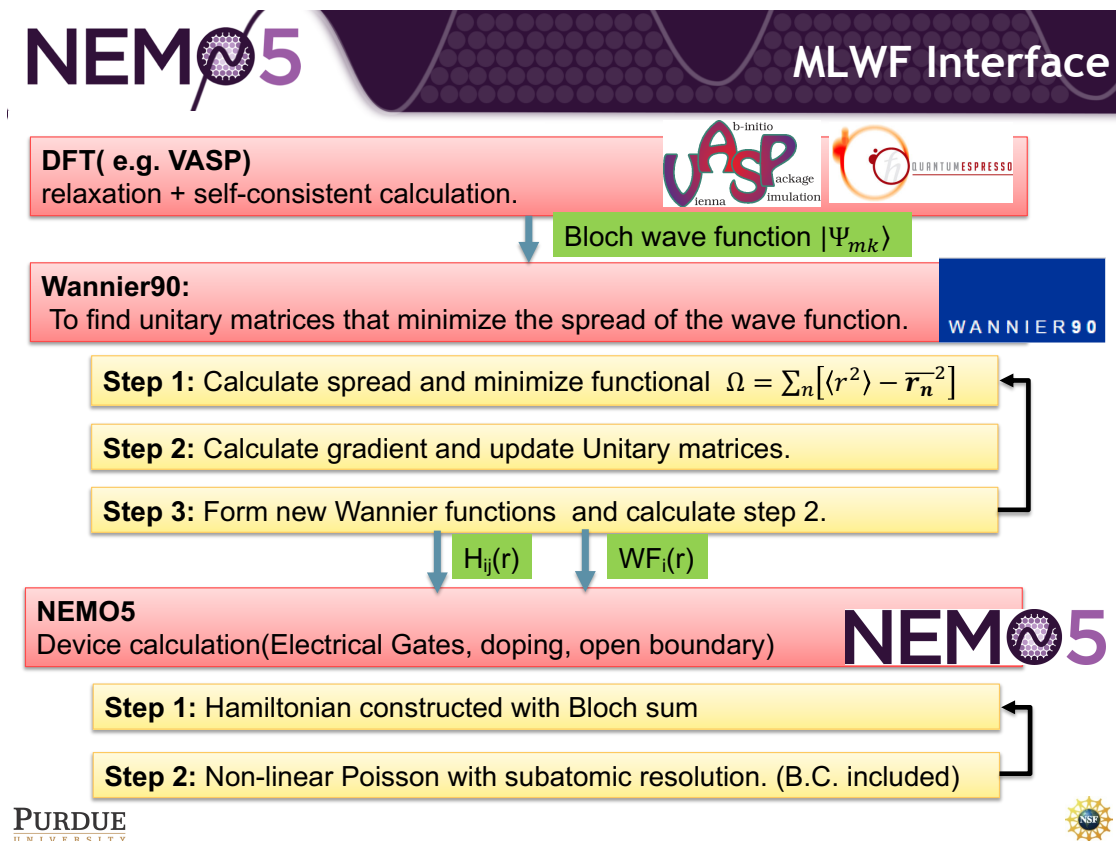
Fig. 2.1.: Flowchart of the MLWF interface in NEMO5.

2.3 TB vs. MLWF comparison

TB and MLWF are compared with DFT data for different layer thickness structure in Fig.2.2. More deviation is found for TB around the Γ valley of the conduction band when more layers are tested on.

2.4 Gaussian charge interpretation with MLWF

Two types of charge interpretation of the atomistic charge is described in Fig. 2.3. Traditionally, delta charge interpolation method will assign the full carrier density in the element atom resides, which becomes a delta function like distribution as we refine the mesh. In the newly implemented Gaussian charge scheme we proposed,
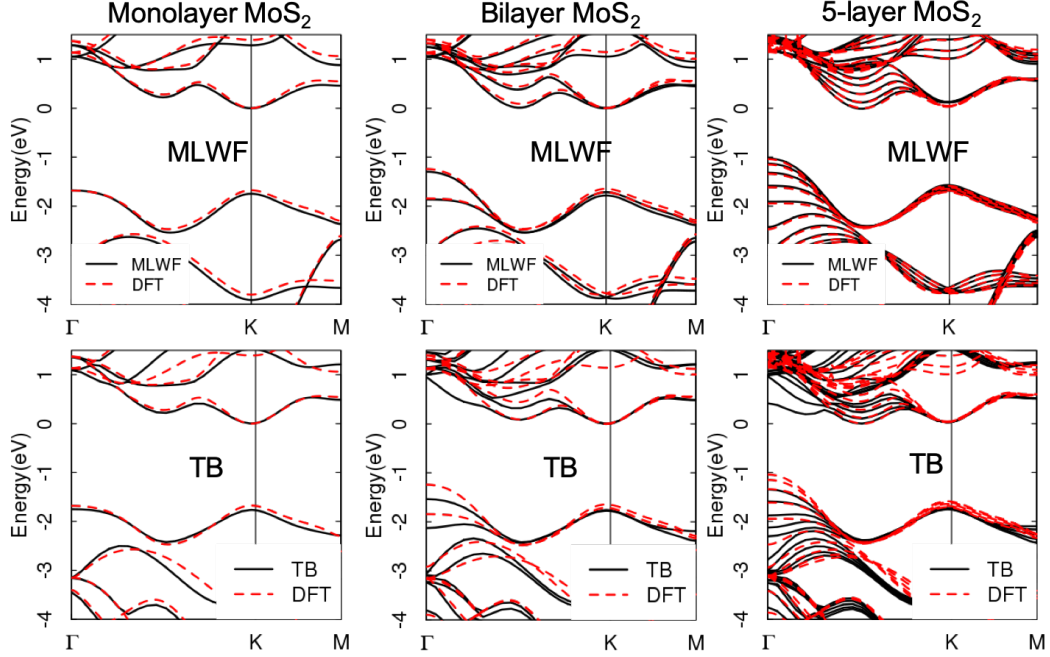
Fig. 2.2.: The band structure comparison between MLWF vs. TB basis for MoS_2 of different layer thickness.

each atom's charge is distributed according to a Gaussian function with a broadening factor σ which will span across multiple elements each assigned the "share" according an integration with the Gaussian function on the FEM cell. The value σ can be further extracted from the ab-initio results of the Wannier function which will be demonstrated in the next Chapter.

With ab-initio method, the device dealt with may be down to a few atoms in dimension. This motivates a finer finite element mesh to provide a better resolution,however, at the expense of convergence and numerical stability. Fig. 2.4 shows the convergence of Poisson for the two methods in the case of monolayer MoS_2 under gate bias with a grid size of around 0.1nm. Fig. 2.5 shows the convergence of Poisson for the two methods in the case of 4 layers MoS_2 under gate bias with refining grid size. Gaussian charge shows convergence of potential result.
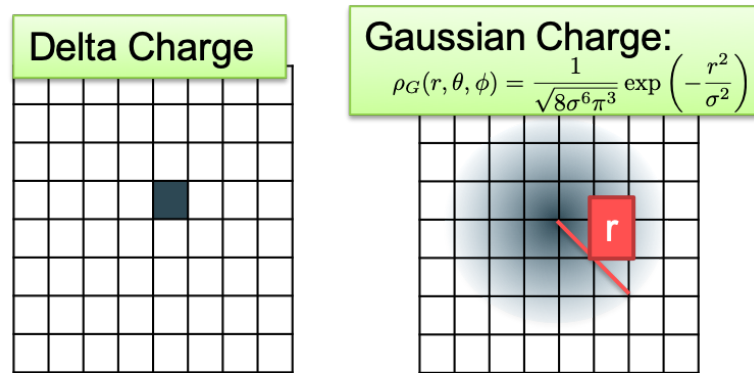
Fig. 2.3.: Schematic showing how atomistic charge is mapped unto finite element mesh.
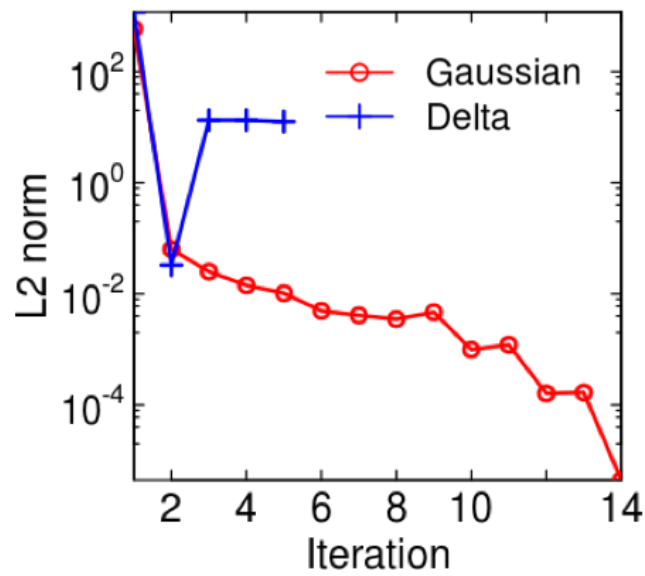
Fig. 2.4.: Convergence comparison between the Gaussian charge and Delta charge interpretation. Poisson's L2 norm is plotted vs. Poisson's iteration number.
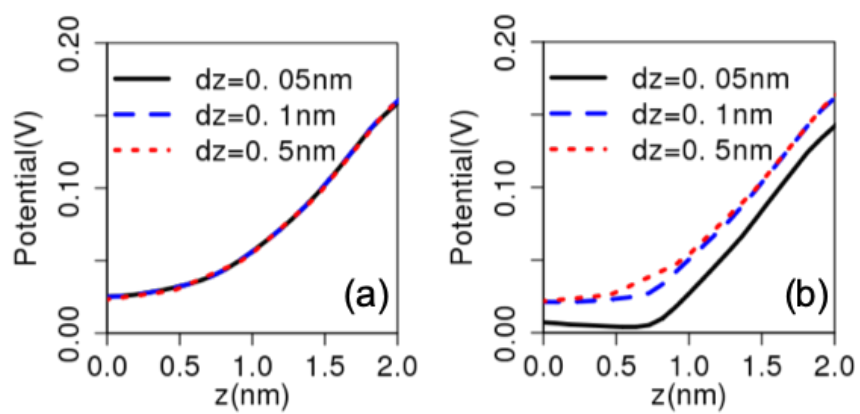
Fig. 2.5.: Convergence comparison between (a) Gaussian charge and (b)Delta charge mapping for different grid size.

3. CONTROL OF INTERLAYER PHYSICS IN 2H TRANSITION METAL DICHALCOGENIDES

Reproduced from "Wang, K. C., Stanev, T. K., Valencia, D., Charles, J., Henning, A., Sangwan, V. K., Kubis, T. (2017). Control of interlayer physics in 2H transition metal dichalcogenides. Journal of Applied Physics, 122(22)" with the permission of AIP Publishing.

3.1 Introduction

Transition metal dichalcogenides (TMDs) are expected to push nanotechnology to the ultimate scaling limit of one or a few atoms only. In contrast to graphene, these 2D materials maintain a native bandgap that is essential for most electronic device applications. TMD based devices have excellent sensitivity to external fields [23–25]. Obvious ultrascaled applications range from sensing (e.g. Refs. [26–29]), lighting (e.g. Refs. [30–32]), logic devices (e.g. Refs. [33, 34]) and wearable electronics (e.g. Refs. [35, 36]).

The weak van der Waals coupling between TMD layers allows for low cost fabrication (with micro-mechanical cleavage [37]) and stacking of different TMD materials on top of each other which significantly widens the material design space [?, 38]. A critical question for most TMD systems is the nature of the coupling between TMD layers. Properties of TMD materials can be tuned via the number of coupled layers. For instance, the band-gap of MoS_2 varies by about 1 eV and switches between direct and indirect when the thickness changes [25]. These features suggested to combine TMD layers of different thicknesses and materials to improve (e.g.) tunneling field effect transistors [39, 40].

In spite of the importance of the interlayer coupling, its detailed properties and dependencies are not fully assessed, yet. For instance, recent experiments on excitons in TMD materials raised the question whether electron hole recombinations are predominantly within the same or between different TMD layers [41, 42]. Depending on the experimental setup, interlayer excitons appear in photoluminesence measurements, while intralayer transitions yield either a finite or a vanishing Stark effect [43, 44]. Given the varying findings in literature, a comparative study of experiments and realistic theoretical models is needed to conclusively assess the interlayer coupling. This is the core purpose of this work.

Although the main focus of this work is the theoretical assessment of the interlayer physics, the reliability of the theoretical answers is assessed with quantitative comparisons of predicted quantum confined Stark effects with experimental observations in various gated MoS_2 structures.

All TMD devices in this work are subatomically resolved. Ab-initio electronic Hamiltonian operators are discretized with maximally localized Wannier functions (MLWF) [18]. This treatment combines numerical efficiency with the best known physical accuracy [45]. In contrast to pure ab-initio models [43], this approach allows to realistically include the presence of electric gates, thickness dependent doping and dielectric constants. Charge effects turn out to significantly influence the interlayer coupling. Commonly, electronic charge distributions are interpreted point-like within the discretization of the Poisson equation [46]. It is an important aspect of this work that these charges are resolved in subatomic resolution as well. These features guarantee full transferability of the electronic model [45, 47] to device dimensions that are computationally inaccessible to pure density functional theory (DFT) applications [48]. Note that important device aspects such as doping densities and spatially varying gate control are beyond the scope of pure DFT applications otherwise [49].

All fabricated devices of this work consist of varying numbers of TMD layers placed on SiO_2 and highly p-doped Si that serves as gate electrode. Our calculations show both interlayer and intralayer excitons yield Stark effects. However, intralayer

transitions are about 2 orders of magnitude less likely. Our experimental data and theoretical predictions for the Stark effect of intralayer transitions agree well. Both theory and experiments do not show significant interlayer transitions.
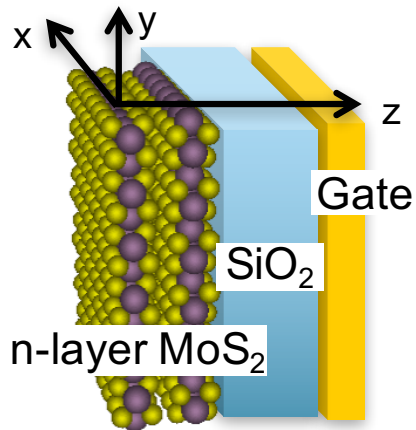
Fig. 3.1.: Schematics of the metal-oxide semiconductor structure considered in this paper. The MoS_2 structure varies in thickness and is limited to the right by the gate and to the left by vacuum.

The paper is organized as follows. In the next section, details of the theoretical model and experimental setup are given. The results section first confirms the transferability of the electronic bandstructure model to the considered devices. It then illustrates and discusses wave function and band structure properties and their dependence on the balance of spin-orbit interaction and interlayer coupling strength. This balance depends on layer thickness, electronic momentum and applied gate fields. The comparison of calculated band gap changes with experimentally observed photoluminesence data confirms Stark effects for both inter and intra layer direct band gap excitons. In agreement with literature, intralayer excitons are found to be significantly more visible.

3.2 Method

3.2.1 Experiment

The device fabrication followed the procedure of Ref. [37]. MoS_2 samples were mechanically exfoliated from bulk MoS_2 crystals and put on 285 nm thick SiO_2 layers that were grown on p-doped silicon substrates (see schematic in Fig. 3.1). Suitable multilayer samples were identified by optical microscopy and their thickness was confirmed independently through atomic-force microscopy. All fabricated samples were first annealed at 300 degrees Celsius to remove residue from the exfoliation process in Ar/H2 environment (800/200 SCCM). The electrostatic gates were defined through e-beam lithography on a MMA/PMMA mask, followed by 100nm deposition of Au via thermal evaporation. Next, the devices were annealed at 200 degrees Celsius (800/200 SCCM, Ar/H2) to clean the substrate of polymer residue from fabrication and improve the contact between metals and semiconductor layers before being loaded into a closed-cycle optical cryostat (Advanced Research Systems DMX-20-OM) [50] and pumped down to high vacuum at 10^{-7} mbar. The devices were kept at 350 K for about 6 hours in high vacuum while laser annealing was applied with a 5 mW beam of a 100 µm spot size. This was meant to help remove atmospheric contaminants, before the samples were cooled down to 10 K, i.e. the temperature at which all measurements were conducted. Photoluminescence measurements were performed using a continuous pump laser beam of 532 nm wavelength with a laser power of 40 µW and a spot size of 2 µm. The emitted light was analyzed with an Andor Shamrock Spectrograph [51] using a 150 lines/mm grating.

3.2.2 Model

The atomic structures of all TMD layers modelled in NEMO5 [52] (i.e. MoS_2, WTe_2, WS_2, WSe_2, and $MoSe_2$) are based on relaxation calculations of the respective infinite number of layers system in trigonal prismatic polytype (i.e., in 2H symme-

Table 3.1.: Structure parameters of all TMD materials resulting from the relaxation and parameterization algorithm described in the main text.

	u ($\mathring{A}$)	a($\mathring{A}$)	c($\mathring{A}$)	range($\mathring{A}$)
MoS_2	3.12	3.18	12.48	20
$MoSe_2$	3.34	3.32	13.14	25
WS_2	3.15	3.19	12.49	23
$MoTe_2$	3.62	3.56	14.22	26
WSe_2	3.36	3.33	13.24	26

try) [25] performed in the DFT tool VASP [53] with the self-consistent electronic model and the convergence criterion of 1×10^{-8} eV. A momentum mesh of 5×5×5 Monkhorst-Pack grids and energy cutoff of 520 eV is used along with van der Waals force included according to Ref. [54]. The lattice constants deduced from these DFT based relaxation calculations are given in Table 3.1 and agree well with the findings in Ref. [55, 56]. The applied DFT model is based on the generalized gradient approximation utilizing the Perdew-Burke-Ernzerhof functionals [57]. The electronic DFT Hamiltonian is transformed into an MLWF representation using the Wannier90 software [?, 58, 59] with d orbitals for the metal electrons and sp^3 orbitals for the chalcogenide electrons as the initial projection. The spreading of the Wannier functions [18] is reduced iteratively until it converges to around 2 $\mathring{A}^2$. Atom positions and their corresponding electronic Hamiltonian of finite TMD structures are then created in NEMO5 [52] as portions of the respective infinite system. As a consequence, all TMD systems in this work are intralayer periodic (in x- and y-direction of the schematic in Fig. 3.1) with Bloch boundary conditions applied. Nonlocal Hamiltonian elements are considered up to the material specific range listed in Table 3.1. All

calculations of gated MoS_2 structures sketched in Fig. 3.1 are performed with self-consistent solutions of the Schrödinger and Poisson equations. The Poisson equation is discretized on a finite element mesh (FEM). The resulting electrostatic potentials converged for FEM resolutions of 0.6Å or better. The electronic density resulting of the solution of the Schrödinger equation is transformed into real space simplifying the MLWF basis with Gaussian functions with σ=0.68 Å (in Eq. 3.1). This simplification eases the numerical burden during the iterative solution of the Poisson and the Schrödinger equation significantly and does not noticeably alter the actual spatial charge distribution as illustrated in Fig. 3.2. This figure shows the integrated charge contribution function $P(r_0)$ in Eq. 3.2 solved with the charge distribution function $\rho(r,\theta,\phi)$ of the MLWF and the fitted Gaussian function $\rho_G(r,\theta,\phi)$ of Eq. 3.1, respectively.

$$\rho_G(r,\theta,\phi) = \frac{1}{\sqrt{8\sigma^6\pi^3}} \exp\left(-\frac{r^2}{\sigma^2}\right) \tag{3.1}$$

$$P(r_0) = \frac{\int_0^\pi \int_0^{2\pi} \int_0^{r_0} \rho(r,\theta,\phi) r^2 sin\phi \, dr d\theta d\phi}{\int_0^\pi \int_0^{2\pi} \int_0^\infty \rho(r,\theta,\phi) r^2 sin\phi \, dr d\theta d\phi} \tag{3.2}$$

The MoS_2 thickness of the gated structure in Fig. 3.1 is varied between one and ten layers. In these cases, the donor doping is set to $1.5 \times 10^{18}\,\text{cm}^{-3}$ for MoS_2 monolayers, $2 \times 10^{19}\,\text{cm}^{-3}$ for 6 MoS_2 layers. The effective doping is induced from the atmospheric adsorbates. Their values are deduced from experimental threshold voltages and gate oxide capacitances [60]. The doping density is linearly interpolated for MoS_2 layer systems in between 1 and 6 layers and it is assumed to be saturated for MoS_2 layers thicker or equal to 6-layers [60]. As commonly done in device calculations [61], the computational burden of 285 nm thick SiO_2 as gate dielectric is avoided with a 12nm dielectric slab of the same equivalent capacitance in the Poisson equation. SiO_2 did not enter the electron density calculations. The gate is considered as a Schottky contact with a metal work function of 5.15 eV [62] for the highly p-doped Si. The energy offset is set to the Fermi level of the device electrons. The uncapped TMD side is considered to be exposed to vacuum, modeled with vanishing field boundary

conditions for the Poisson equation. The MoS_2 dielectric constant is assumed to be homogeneous but linearly varying with the layer thickness following Ref. [63]. The electronic wave functions of the conduction and the valence band states are used to solve the optical transition matrix elements. Peaks in these optical elements are considered as optical transition energies [64]. For all gate-independent bandstructures and wave function assessments in this work, a constant doping of $1.5 \times 10^{18} \, cm^{-3}$ is assumed and the Fermi level is chosen to achieve local charge neutrality for the respective systems. The electron hole recombination energies are extracted from single particle bandstructures. As discussed in Ref. [65], many particle effects are expected to have in low order no net impact on the transistion energies.
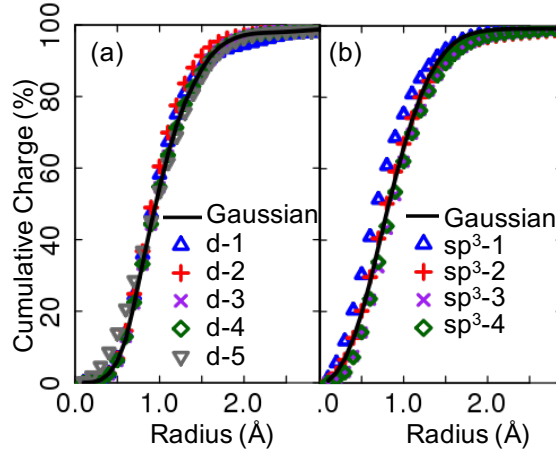
Fig. 3.2.: Integrated charge contribution function $P(r_0)$ as defined in Eq. 3.2 as a function of the integration radius for orbitals of molybdenum (a) and sulfur (b) atoms in infinitely thick MoS_2. The black lines show $P(r_0)$ when the orbital wave functions are approximated with Gaussian functions of $\sigma = 0.68 \mathring{A}$ (a) and $\sigma = 0.6 \mathring{A}$ (b), respectively.
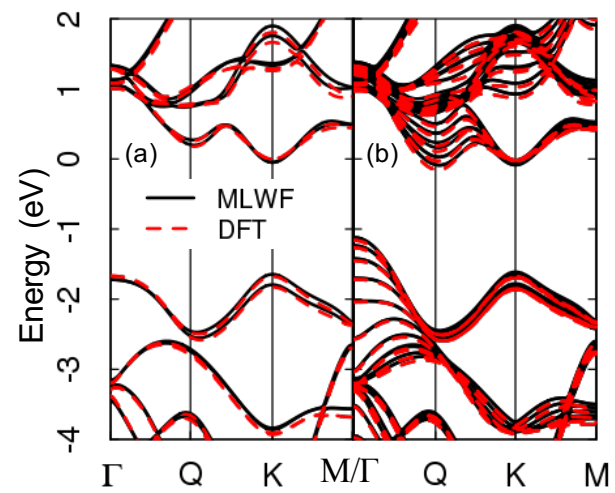
Fig. 3.3.: Comparison of mono-layer (a) and quintuple layer (b) MoS_2 band diagrams solved with MLWF in NEMO5 and the DFT functionality of VASP. The agreement confirms the transferability of the MLWF parameters.
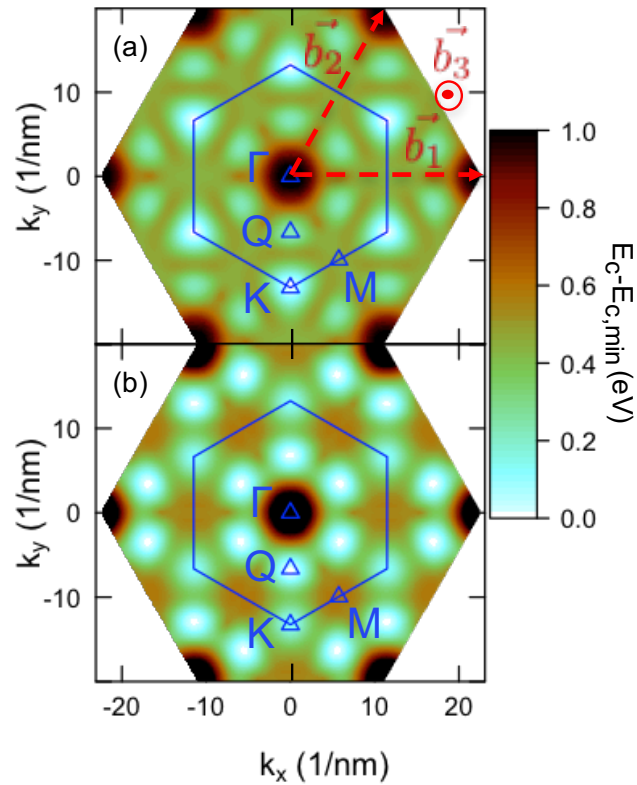
Fig. 3.4.: Contour graph of the conduction band minimum of mono-layer (a) and 5-layer (b) MoS$_2$. The blue hexagon depicts the first Brillouin zone. Reciprocal lattice vectors are labeled with $\vec{b_1}$, $\vec{b_2}$ and $\vec{b_3}$. Note that the location of the Q valley is close to the middle between K and Γ.

3.3 Result

3.3.1 Transferability of MLWF parameters

The NEMO5-calculated bandstructures in the MLWF representation agree well with the ab-initio results of the VASP software [25] for any MoS_2 layer thickness (see Fig. 3.3 for the monolayer and 5-layer cases). Very similar transferability of the MLWF representation and fitting procedure was found for all other TMD materials and layer thicknesses. This is remarkable, since MLWF parameterizations are sometimes created for each material thickness individually [45].
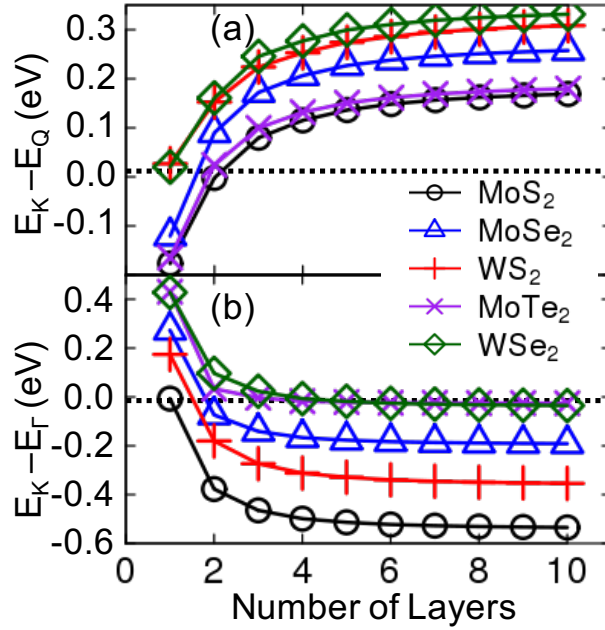
Fig. 3.5.: Valley energy differences in the conduction band (K and Q valley) (a) and valence band (K and Γ valley) (b) as a function of the TMD layer thickness.
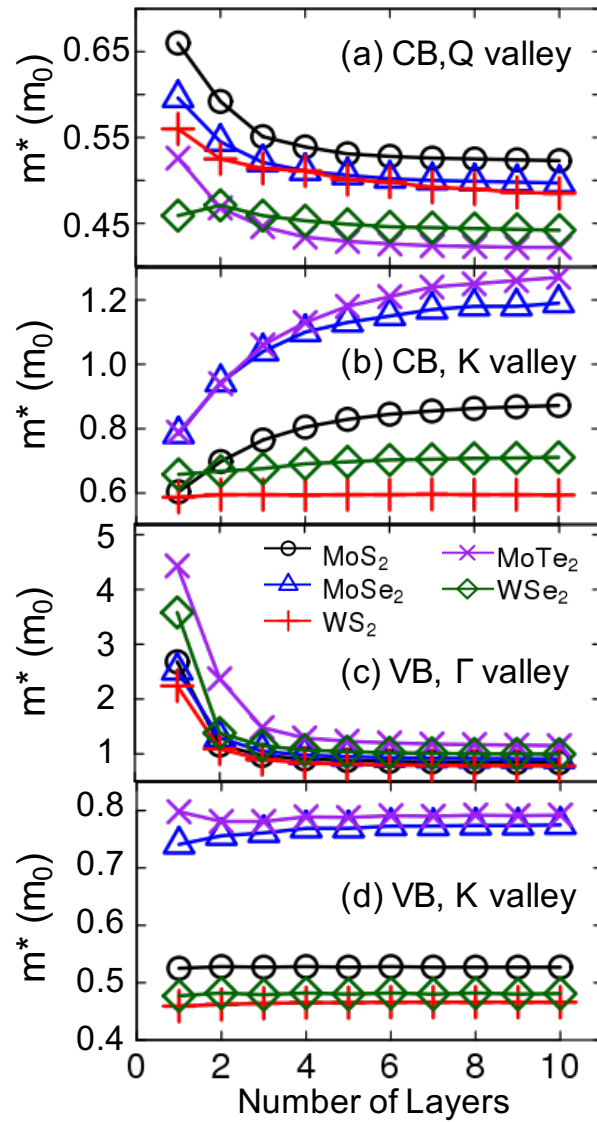
Fig. 3.6.: Calculated effective masses along the $\vec{b_1} - 2\vec{b_2}$ direction for the conduction band Q (a) and K valley (b), as well as for the valence band Γ (c) and K valley (d).

3.3.2 Conduction and valence band energies and masses

The conduction band minimum in 2D momentum space for monolayer and 5-layer MoS_2 are shown in Figs. 3.4. For all TMDs considered in this work, the lowest conduction band hosts valleys at the K points and close to the Q points, respectively. Note that each K-point (Q-point) contributes to 3 (1) Brillouin zones and therefore its valley is twofold (sixfold) degenerate. Similarly, all considered TMDs show two valleys in the highest valence band at the Γ point and at the K-point [25]. The relative energies of all these valleys depend on the layer thicknesses, as illustrated in Figs. 3.5 (a) and (b) for conduction and valence bands, respectively. Most of the TMDs show a transition of the conduction band minimum (valence band maximum) from K to Q (K to Γ) valley at around 2 layer thickness [66, 67]. The valley effective masses change with layer thickness as well (see Fig. 3.6) - very similar to findings of Ref. [25] for MoS_2.

3.3.3 Band edge density of states

For a 2D system, the density of states (DOS) will be proportional to the effective mass. Note that the Q valley conduction band DOS decreases for all TMDs with increasing layer thickness as a direct consequence of the effective mass behavior. In the valence band, the Γ valley effective masses decay with thickness, while the K valley masses stay fairly constant (see Figs. 3.6 (c) and (d)). The energies of K- and Q-valleys for two layer n-type TMDs are close enough so that both valleys contribute to the DOS at the band edge. Once the Q-valley of n-type TMDs (i.e., MoS_2 [68], $MoSe_2$ [69], WS_2 [70]) is significantly lower in energy than the K-valley (e.g., for more than 2 layers in the case of MoS_2), the DOS at the conduction band edge reduces with increasing layer thickness following the effective mass trend. This is exemplified in Fig. 3.7 which shows the DOS of MoS_2 with varying layer thickness.

To illustrate the DOS behavior for all considered n-type (p-type) TMDs and thicknesses Fig. 3.8 (a) (Fig. 3.8 (b)) shows the effective Fermi level $E_f - E_c$ ($E_v - E_f$)
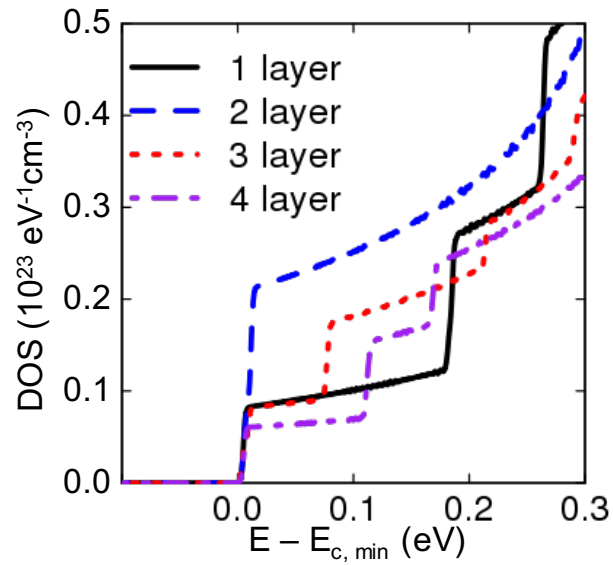
Fig. 3.7.: Conduction band density of states in MoS_2 layers of various thicknesses. The 2 layer system has the largest DOS due to the alignment of K and Q conduction band valleys. Each step in the DOS marks an onset of a higher conduction band. The finite slope of the DOS between each step originates from a non-parabolic band dispersion.
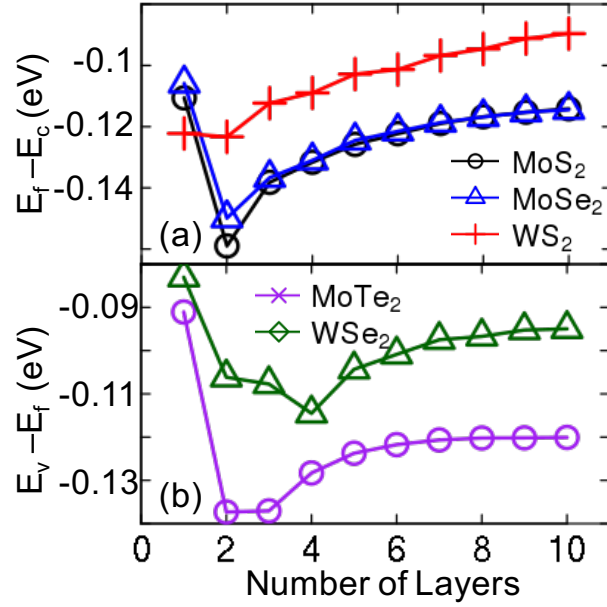
Fig. 3.8.: Effective Fermi level $E_f - E_c$ (a) and $E_v - E_f$ (b) of n- and p-type TMD layers with varying thickness and for a given doping density of $1.5 \times 10^{18}\ \mathrm{cm^{-3}}$, respectively.
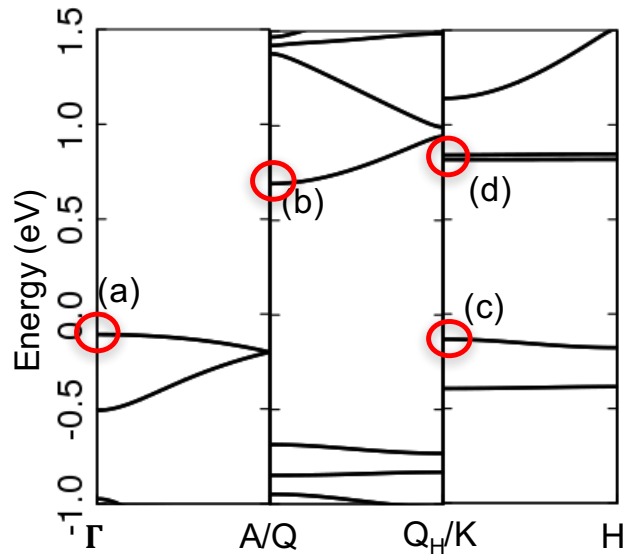
Fig. 3.9.: MoTe$_2$ band diagram along $\vec{b_3}$ starting at the Γ, Q, and K points defined in Fig. 3.4. A, Q$_H$ and H points correspond to Γ, Q, and K when shifted by $\pi/c \times \vec{b_3}/|b_3|$.
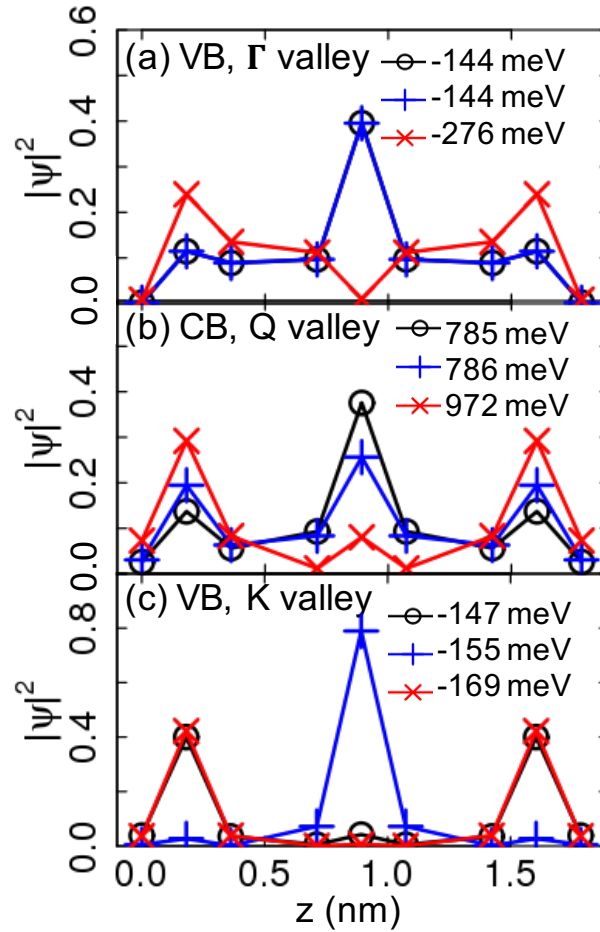
Fig. 3.10.: Absolute squared valence band wavefunctions for Γ valley of the valence band (a), Q valley of the conduction band (b) and K valley of the valence band (c) of a 3 layer MoTe$_2$ system corresponding to the points (a), (b) and (c) in Fig. 3.9, respectively. The eigenstate energy is used to label the states. Depending on the interlayer and spin orbit coupling strength, the wavefunctions are localized or delocalized. Note that the lines are meant to guide the eye.

assuming a constant electron (hole) density of $1.5 \times 10^{18}\,\mathrm{cm^{-3}}$. Note that the larger the electron (hole) DOS is around the conduction band minimum (valence band maximum), the lower the effective Fermi level has to be to maintain the assumed density. All n-type TMDs except WS$_2$ show a maximum DOS at 2 layers thickness when both K- and Q-valleys contribute. The p-type TMDs show a maximum DOS at 2 and 4 layers for MoTe$_2$ and WSe$_2$, respectively. This is the situation when both the Γ and the K valleys similarly contribute to the DOS around the Fermi level.

3.3.4 Interlayer hybridization

2H-phase TMDs consist of alternating layers with 2 different orientations of metal-chalcogenide bonds (differing in a 60° rotation) [71, 72]. If the electrons are subject to a pronounced spin-orbit interaction (e.g., in odd-layer 2H-TMD systems without inversion symmetry [72–75]), electronic states spreading across alternating layers are suppressed [76, 77]. In contrast, the geometrical confinement favors electronic states that are spread across the total device if the interlayer coupling is strong enough [78]. Figure 3.9 shows the bandstructure of an infinite layer MoTe$_2$ system at various symmetry points of the 2D momentum space along $\vec{b_3}$ direction. The stronger the interlayer coupling, the stronger curved the respective bands in Fig. 3.9 are. In Fig. 3.9 several points in the bandstructure are labeled. They face different balances between the interlayer coupling strength and the spin-orbit interaction: At the valence band Γ point (labeled with (a)), the spin-orbit interaction vanishes and only the interlayer coupling determines the shape of the electronic wave functions. Here, this coupling is significant and gives an effective mass of -2.31m$_0$ for the top of the valence band. Consequently, the highest valence band states resemble typical infinite-barrier quantum well shapes (note they are spin degenerate, see Fig. 3.10 (a)). At the Q-point of the conduction band (labeled with (b) in Fig. 3.9) the spin-orbit interaction is finite but smaller than the strong interlayer coupling (effective mass m* = 0.53 m$_0$ at Q along $\vec{b_3}$ direction). Consequently, the shape of the electronic states shown in

Fig. 3.10 (b) is still comparable with those of Fig. 3.10 (a), but the spin degeneracy is lifted. The top-valence band states at the K-point (labeled (c) in Fig. 3.9) face similarly strong interlayer coupling (effective mass $m^* = -1.68m_0$ at K along K-H direction) and spin-orbit interaction. Consequently, the respective wave functions avoid spreading in alternating layers. Instead, states of equivalent layers (i.e., next-nearest neighbor layers) hybridize into bonding and anti-bonding states. In the case of a 3-layer system, states of only two layers can follow that (depicted in Fig. 3.10 (c) with circles for the bonding state and crosses for the antibonding state), while states of the center layer (symbol "+" in Fig. 3.10 (c)) are effectively isolated. In agreement with Ref. [72] the lowest conduction band states at the K-point (labeled with (d) in Fig. 3.9) is found to have a very small interlayer coupling (effective mass $m^* = -699m_0$ at K along $\vec{b}_3$ direction), i.e., a coupling smaller than the respective spin-orbit interaction. Therefore, electronic states of individual layers barely interact and are effectively degenerate. Note that the spin-orbit interaction does not play a significant role in systems with inversion symmetry (i.e., with an even number of layers). Very small spin-orbit coupling effects observed in these systems can be addressed to small p-orbital contributions of chalcogenide atoms to the conduction band [74]. Then, wave functions are exclusively determined by the interlayer coupling strength. It is worth to emphasize that the wave function effects discussed above are found in all considered TMD materials.

3.3.5 Electric gate response

The effect of electric gates on TMD layers is exemplified with the absolute squared conduction band wave functions and the self-consistently solved electrostatic potential of a 6-layer gated MoS_2 system shown in Figs. 3.11. The energies of K-valley and Q-valley states get closer with the electric field: in the field free case, the bottom of K and Q valleys are separated by more than 100 meV, whereas their energy difference is about 58 meV, as seen in Fig. 3.11. Higher gate fields make it energetically more
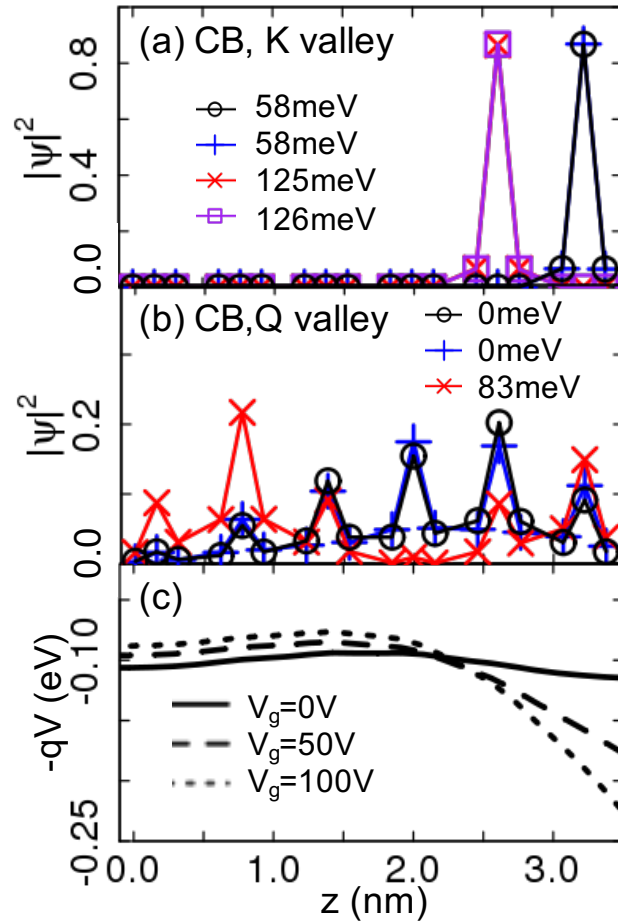
Fig. 3.11.: Absolute squared of several conduction band wave functions at the K point (a) and at the Q point (b) for a 6-layer gated MoS_2 device depicted in Fig. 3.1 at a gate voltage of $V_g = 100\,V$. The MoS_2 system extends from $z = 0\,nm$ to $z = 3.6\,nm$. The potential profiles for various gate voltages are shown in (c). The lines in (a) and (b) are meant to guide the eye.

favorable to avoid state delocalization across the total device. This can be seen for the Q-valley states in Fig. 3.11 (b) as their center shifts in the gate field direction. The electrostatic potential profiles for several different gate voltages are shown in Fig. 3.11 (c). In these and all other considered cases of this work, the gate field is screened within about 1 nm penetration depth. Consequently, the thinner the TMD system is, the larger is its response to the applied gate field. This is exemplified in Fig. 3.12 for the effective Fermi level as a function of gate bias and layer thickness. Note that the monolayer results of this figure still assume completely screened gate field in the vacuum, in spite of the pronounced penetration depth. Thus the monolayer results are given for the sake of completeness only and to ease comparison with the effective Fermi levels shown in Fig. 3.8. For higher gate fields and TMDs thicker than the field penetration length, the gate induced shift of effective Fermi level becomes independent of the layer thickness (see Fig. 3.12). Since K-valley states are localized within monolayers, they face a layer-dependent effective electric field. Accordingly, the K-valley degeneracy gets lifted by electric gates, as illustrated in Fig. 3.11 (a) and Fig. 3.13. Note that the Q-valley conduction band energies and Γ valley valence band energies remain virtually unaffected by the electric gate (see Fig. 3.13).

3.3.6 Quantum confined Stark effect

Figure 3.13 also shows that the quantum confined Stark effect of the K-valley states reduces the direct band gap at the K-point. Similar effects were observed for direct band gap excitons in Ref. [44,80] as well as in the experiments of this work: the photoluminesence peaks of direct band gap excitons show a red-shift with increasing gate voltage (see Fig. 3.14). Figure 3.14 also shows an increase of the PL amplitude with increasing gate bias. This qualitatively agrees with the bandstructure results of Fig. 3.13: The gate field barely changes the K-valley valence band edge, but it lowers the K-valley energy of the conduction band. This results in an increase of the K-valley electron density with the gate bias, while the K-valley hole density is approximately
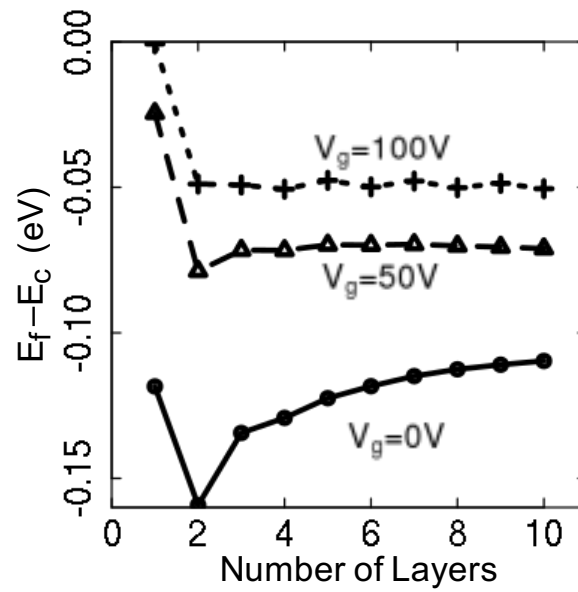
Fig. 3.12.: Effective Fermi level of the gated MoS_2 layers shown in Fig. 3.1 for different thicknesses and applied gate voltages. For this comparison a layer thickness independent doping density of $1.5 \times 10^{18} \, cm^{-3}$ is assumed.
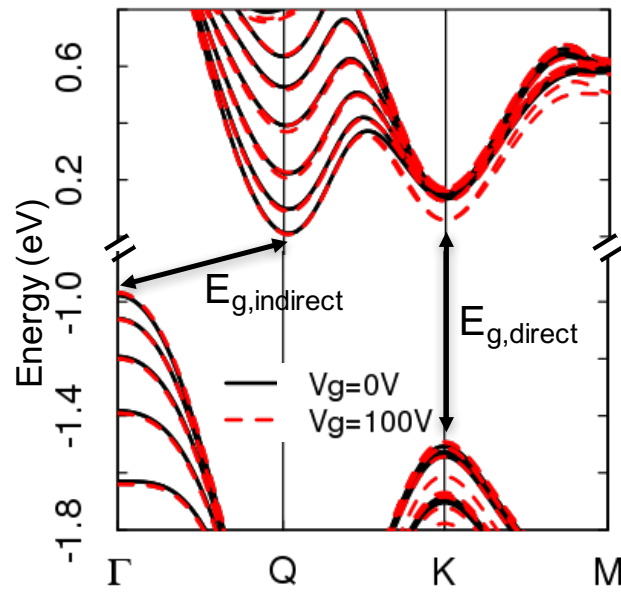
Fig. 3.13.: Bandstructures of a 6-layer MoS$_2$ system as shown in Fig. 3.1 for the field free case and when a gate voltage of 100 V is applied. The gate field lifts the K valley degeneracy while the Γ and Q valleys remain virtually unaltered. To ease the comparison, the energy offset is chosen to have the Fermi level set to 0 for both voltages.
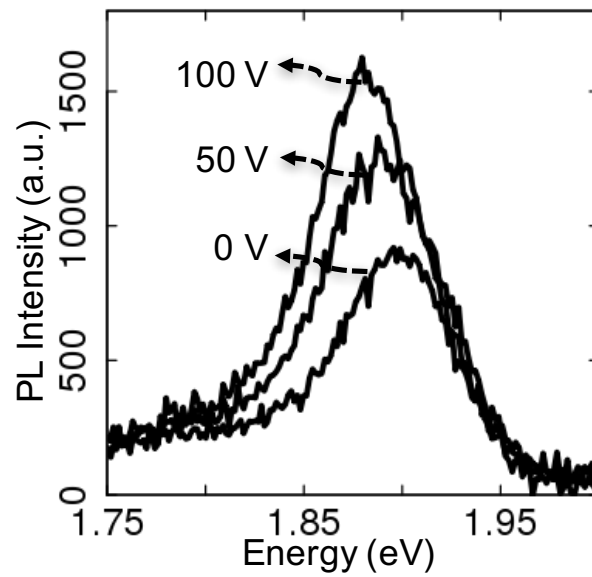
Fig. 3.14.: Experimental photoluminescence (PL) spectra (equivalent to "peak A" in Ref. [79]) of a gated 6 layer MoS_2 structure for various gate voltages. The increase of the PL amplitude with the gate voltage qualitatively agrees with band structure changes predicted in Fig. 3.13 as discussed in the main text.
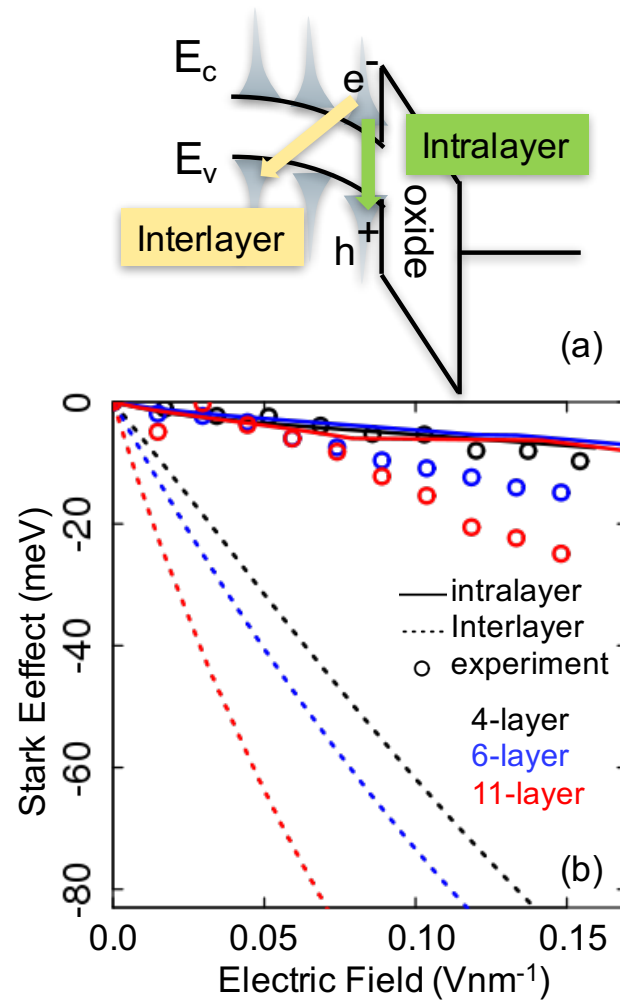
Fig. 3.15.: (a) Schematic of the interlayer and intralayer exciton recombinations. (b) The relative change of experimentally observed direct band gap exciton energies (symbols) as a function of applied gate bias for various MoS_2 systems agrees well with the theoretically predicted energy differences of conduction and valence band K-valley states of identical layers (solid lines). In contrast, the calculated conduction and valence K-valley energy differences of maximally separated layers (dotted) significantly exceed the experimentally observed Stark effects.

constant. Since the photoluminescence amplitude is approximately proportional to the product of electron and hole K-valley density (see e.g. Ref. [81,82]), it increases with the gate bias.

It had been discussed in literature (Ref. [42–44]) whether the direct band gap excitons are recombining within individual layers or across different layers (illustrated in Fig. 3.15 (a)). To clarify the nature of the excitons and shed more light on this question, Fig. 3.15 (b) compares the field induced changes of the experimentally observed exciton energies with NEMO5 results. Since the NEMO5 calculations do not include exciton binding energies, differences of K-valley conduction and valence band states of the same layer and of maximally separated layers are used to represent intralayer and interlayer excitons, respectively. For comparability of experimental and NEMO5 results, the transition energy changes in Fig. 3.15 (b) are shown relative to the field free case. For both, the interlayer and intralayer transitions NEMO5 predicts a finite Stark effect, but only the intralayer transition Stark effects agree qualitatively with the experimental data. Note that NEMO5 calculations of the optical matrix elements [83] (not in the figure) showed two orders of magnitude higher probability for intralayer transitions then for interlayer ones. It is also worth to mention that our experiments did not show any Stark effect for indirect band gap excitons - in agreement with the theoretical results in Fig. 3.13 that show virtually gate field independent Q-valley and Γ-valley energies. In summary, these results suggest that MoS_2 excitons preferably perform intralayer transitions.

3.4 Conclusion

Electronic wave functions and bandstructures in 2H-TMD structures were analyzed in the MLWF representation of the nanodevice simulation tool NEMO5. Hybridization of electronic states across multiple layers was shown to depend on the balance of spin-orbit coupling and interlayer coupling strength. This balance varies strongly with the electronic momentum. Conduction band K-valley states are found

to be confined in individual monolayers. In contrast, valence band K-valley states are delocalized in equivalent layers for systems with finite spin-orbit coupling or across the total device when the spin-orbit coupling disappears. This K-state hybridization can be lifted with electric gate fields. The design range of the spin-orbit interaction, the interlayer coupling, the effective Fermi levels and effective masses are carefully assessed. Experimental data of the quantum confined Stark effect of direct band gap, interlayer and intralayer exciton photoluminesence were reproduced with NEMO5. Intralayer excitons were identified as the major source for photoluminesence signals - in agreement with a previous study Ref. [44].

4. CARRIER TRANSPORT METHODS

Carriers transport through the device can be observed as current. Different models have been proposed depending on the interpretation of the carriers. Semiclassically, electrons are considered as particles undergone drift force from the Couloumb force and diffusion force due to the density gradient. In the quantum picture, electrons are waves like entity described by Schroedinger equations. This chapter will give a brief introduction of different models and describe the proposed novel model, the BPRG method. A summary of different methods can be found in Fig. 4.1.
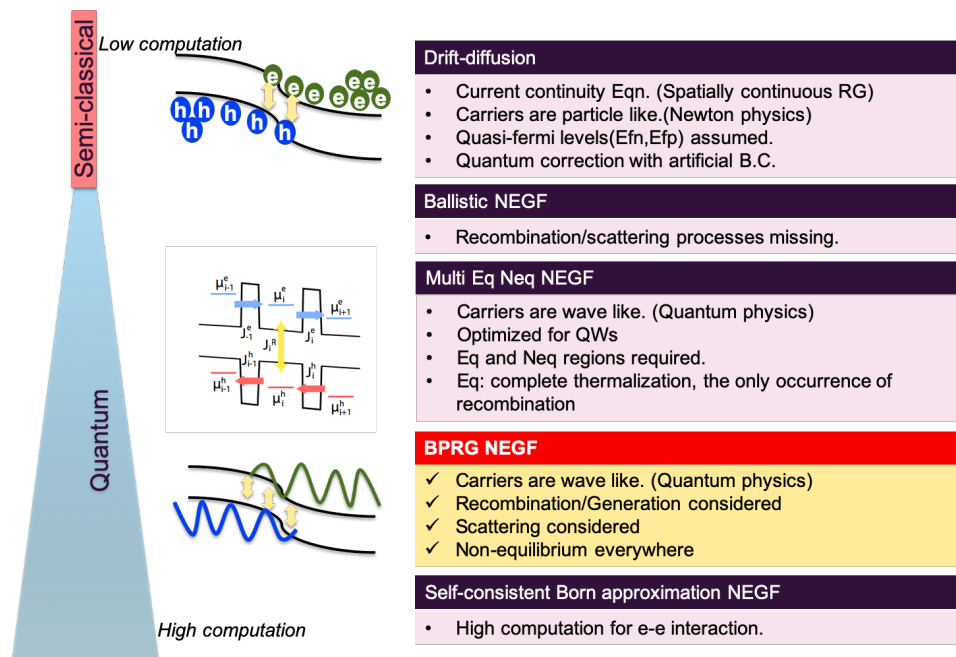
Fig. 4.1.: A summary of different methods for charge transport calculation for electronics.

4.1 Semiclassical Drift Diffusion Model

Drift-diffusion equation [84] is derived from Boltzmann transport equations(BTE) by taking the moments for current [85]. Electron and hole currents each has contribution from the potential gradient resulted drift current, and the density gradient resulted diffusion current.

$$J_n = qn\mu_n\nabla V + qD_n\nabla n \tag{4.1}$$

$$J_p = qp\mu_p\nabla V - qD_p\nabla p$$

Note that $\mu_n(\mu_p)$ stands for the mobility for electron(hole). n(p) is the electron(hole) carrier density. The $D_n(D_p)$ is the diffusion coefficient for electron(hole).

Next the 0'th moment of the BTE is assumed to be time independent, continuity equations conserve the particles in the device given recombination(R) and generation(G):.

$$\frac{1}{q}\nabla J_n - R_n + G_n = 0 \tag{4.2}$$

$$-\frac{1}{q}\nabla J_p - R_p + G_p = 0.$$

Last, Poisson equation has to be satisfied and self-consistently solved for the charge density and the spatial potential.

$$\nabla^2 V = q(-n + p - N_A + N_D) \tag{4.3}$$

4.2 State of art MEQNEQ solver

4.2.1 Overview

Due to the difficulty of NEGF with inelastic scattering, recombination required to simulate LED devices, Multi-scale-Equilibrium-noneQuilibrium (MEQ) has been proposed [16] .

A device example is shown in Fig.4.2 with the total device separated into equilibrium and non-equilibrium regions.
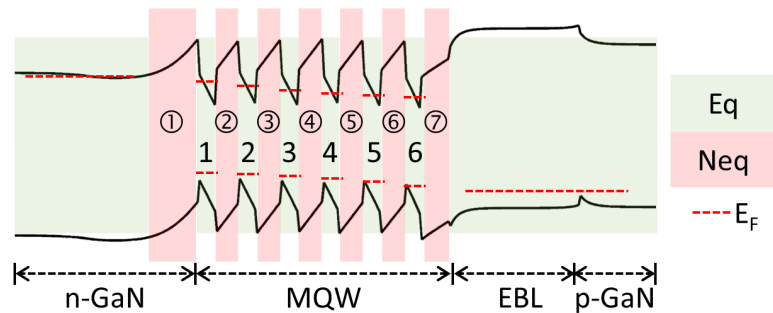
Fig. 4.2.: LED structure that consists of an n-GaN layer; a low-doped active region made of InGaN/GaN MQW; an AlGaN electron-blocking layer and a p-GaN layer. The equilibrium (eq–green) and non-equilibrium (neq–red) regions are marked in different colors. Each eq-region has a unique quasi Fermi level, for holes and electrons as indicated by a red dashed line. [16]

Poisson equation

In the equilibrium region, carriers fill the DOS(calculated from G^R) following Fermi-distribution with quasi-Fermi levels unknown beforehand. In the non-equilibrium region, NEGF ballistic transport is calculated with carriers injected from the neighboring equilibrium regions and the carrier density is distributed as $G^<$.

Current conservation

In the equilibrium regions, Shockley-Read-Hall(SRH), radiative, and Auger recombinations are relevant known as the ABC models [81]. The A is an important paramters for the SRH process where it's inverse, τ_N and τ_P, is the SRH lifetime.

$$J_{j,A} = \frac{n_j p_j - n_{intri}^2}{\tau_N(n_j + n_{intri}) + \tau_P(p_j + n_{intri})}$$

$$\tau_N = \tau_P = 1/A(sec)$$

$$J_{j,B} = B_j \cdot n_j p_j \tag{4.4}$$

$$J_{j,C} = C_j \cdot (n_j^2 p_j + p_j^2 n_j)$$

$$J_{j,total}^R = J_{j,A} + J_{j,B} + J_{j,C}$$

For the current conservation loop, a derivative over Fermi level is needed and derived as an example:

$$\frac{dJ_{j,A}}{dE_f n} = \frac{dJ_{j,A}}{dn}\frac{dn}{dE_{fn}}$$

$$= \left(\frac{p_j}{\tau_N(n_j + n_{intri}) + \tau_P(p_j + n_{intri})} - \frac{n_j p_j - n_{intri}^2}{(\tau_N(n_j + n_{intri}) + \tau_P(p_j + n_{intri}))^2}(\tau_N)\right)\frac{dn}{dE_{fn}}$$

$$= \frac{p_j(\tau_N(n_j + n_{intri}) + \tau_P(p_j + n_{intri})) - (n_j p_j - n_{intri}^2)(\tau_N)}{(\tau_N(n_j + n_{intri}) + \tau_P(p_j + n_{intri}))^2}\frac{dn}{dE_{fn}}$$

$$\tag{4.5}$$

In the non-equilibrium regions, ballistic currents are calculated. All current types need to conserve the particles by adjusting the quasi-Fermi level in each equilibrium regions as shown in Fig.4.3.
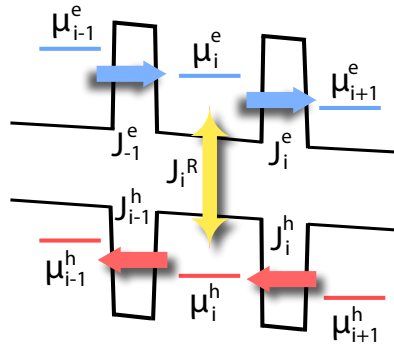
Fig. 4.3.: Schematic diagram of various current component in a single section of LED. Local Fermi levels need to adjust so that overall current is conserved. [16]

4.2.2   Limitations of MEQNEQ

In the MEQ model, carriers are assumed to be fully thermalized in each equilibrium regions. This has been justified by calculating the tunneling rates across the next nearest wells for some biases. However, for higher biases, the assumption can break down and become more unreasonable.

MEQ is designed for commercialized GaN LED structures with barriers between each well. This requires alternating equilibrium and non-equilibrium regions which limit the study for 2D material where there is only vacuum between p and n regions. This also prevents the addition of self-energy in the barrier where interface roughness scattering and band tail study is required.

For the needs to complete NEGF recombination modeling and provide LED industry with the proper TCAD tool, a general model without above mentioned constraints is needed.

4.3   Novel modifications of Büttiker probe

4.3.1   Overview

NEGF equations serve the purpose to models coherent and incoherent transport with atomic resolution however, numerically expensive in incoherent scattering process. Büttiker method was proposed by Markus Büttiker in 1988 with a heuristic but computationally efficient alternative to the self-consistent Born approximation [86]. Later revived and organized [87] with application on the transistor modeling [88]. The method also has application on bosonic particles like phonon regarding the heat transport [89].

4.3.2   Büttiker probe method

The formalism of Büttiker probe [90] can be summarized in the following equations as an alterations from the NEGF formalism from Ref. [91] chapter 8 and Ref. [92]

chapter 19. The index j stands for contacts including source, drains and regionally defined probe contacts. The subscript n and p define the carrier types to be electrons and holes. The equations are iterated such that each regional probes has a zero net current by adjusting the quasi-Fermi levels, μ_{nj} and μ_{pj}. This ensures particles to lose energy due to the scattering process however conserving the number of carriers [87].

The NEGF with Büttiker probe can be illustrated for electron with the following equations. Energy resolved retarded Green's function is a quantity proportional to the density of states in the device with H being the device Hamiltonian

$$G^R(E) = (EI - H - \Sigma_S^R - \Sigma_D^R - \Sigma_\eta^R)^{-1}. \tag{4.6}$$

Energy resolved lesser Green's function corresponds to carrier densities influenced by contacts in their equilibrium states.

$$G^<(E) = G^R(E)\Sigma^<(E)G^{R\dagger}(E) \tag{4.7}$$

The lesser self-energy is implemented here as a diagonal matrix modified by a Fermi distribution.

$$\Sigma^<(E) = \frac{1}{-i}\sum_j [f_j(E)\Gamma_j(E)] \tag{4.8}$$

$$f_j(E) = \frac{1}{exp(E - \mu_{nj}) - 1} \tag{4.9}$$

Due to the RGF formalism, device is partition into nearest coupling slab. The current for each slide through the Büttiker probe is calculated by Eqn. (4.12) , the equivalence of this equation but using transmission is done with [88] however utilizing the full G^R in Eq(10).

$$\Gamma_j(E) = i(\Sigma_j^R(E) - \Sigma_j^{R\dagger}(E)) \tag{4.10}$$

$$I_{nj}(E) = \frac{-i}{h}Trace[\Sigma_j^<(E)A(E) - \Gamma_j(E)G^<(E)] \tag{4.11}$$

$$I_{nj} = \int I_{nj}(E)dE \tag{4.12}$$

The equivalent sets of equation for holes are listed in the following.

$$G^R(E) = (EI - H - \sum_j \Sigma_j^R)^{-1} \tag{4.13}$$

$$G^>(E) = G^R(E)\Sigma^>(E)G^{R\dagger}(E) \tag{4.14}$$

$$\Sigma^>(E) = \frac{1}{i}\sum_j [(1 - f_j(E))\Gamma_{jj}(E)] \tag{4.15}$$

$$f_j(E) = \frac{1}{exp(E - \mu_{pj}) - 1} \tag{4.16}$$

$$\Gamma_j(E) = i(\Sigma_j^R(E) - \Sigma_j^{R\dagger}(E)) \tag{4.17}$$

$$I_{pj}(E) = \frac{i}{h}Trace[\Sigma_j^>(E)A_{j,j}(E) - \Gamma_j(E)G_{j,j}^>(E)] \tag{4.18}$$

$$I_{pj} = \int I_{pj}(E)dE \tag{4.19}$$

Newton method is therefore used to minimize the current in each probe by adjusting the Fermi levels in each probe. The Jacobian matrix can be calculated where $dG^<$ is the main contribution to the off-diagonal term.

$$J_{jm} = \frac{dI_j}{dE_{f,m}} = \frac{i}{h}Trace[\frac{d\Sigma_j^<(E)}{dE_{f,m}}A_{j,j}(E) - \Gamma_j(E)\frac{dG_{j,j}^<(E)}{dE_{f,m}}] \tag{4.20}$$

The Jacobian and the residual vector can be multiplied to generate the difference for next iterations' Fermi-level.

$$\mu_{n,t+1} = \mu_{n,t} + J^{-1}(I_p) \tag{4.21}$$

4.3.3 BP for recombination and generation (BPRG method)

By creating two types of carriers, electrons and holes are solved with traditional BP individually. However, each probe no longer has zero net current as setting Eqn. 4.12 and Eqn. 4.19 to zero but a finite value following Eqn. 4.22.

$$I_{nm} = I_{pm} = J_{m,total}^R + J_m^G \tag{4.22}$$

This problem can be transformed into a minimization problem to look for $[R_m]$ such that the following equations are fulfilled.

$$Residual = R_m - F(n(R_m), p(R_m)) = 0 \qquad (4.23)$$

$$R_m(Efn, Efp) - F(n(Efn), p(Efp)) = 0 \qquad (4.24)$$

A toy example of a quantum well structure is given and shown in Fig. 4.4. The electron is injected from the right end with a Fermi-level of 1.1eV while holes from the right with -1.1eV. The carrier density is shown to peak in the well with a corresponding higher recombination rate as shown in Fig. 4.4(b).

4.3.4 BPRG implementation

Fig. 4.5 is a flow chart showing the interactions of program implemented in NEMO5.

4.3.5 Recursive Green's function with adaptation of Büttiker probe

RGF is a method to solve the inverse for the the Green's function due to the tri-block diagonal form of the matrix. However, the inverse operation is expensive and usually scale as $O(N^3)$. When only the diagonal is calculated, it can be reduced to O(N). The memory consumption can be greatly reduced from $O(N^2)$ to $O(N)$ when only storing the diagonal part of the matrix.

Different types for RGF are used [93–95] when some are efficient but limited to non-scattering while some requires more computation dealing with the scattering.

In order to calculate the gradient of probe current versus probe Fermi level, [96] has derived in the paper's Eqn.(10)-(13).
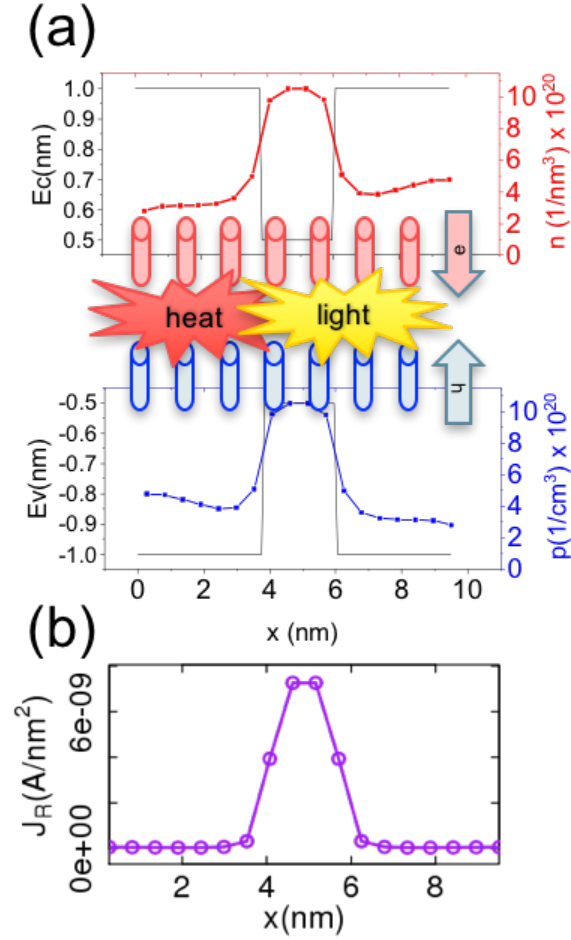
Fig. 4.4.: A V=0 quantum well scenario with Büttiker probe recombining carriers. (a) E_c, E_v, electron density and hole density. (b) Showing carrier recombination at each position of the device.

4.3.6 Device self energy

In Eq. (4.6), Σ_η^R is the self-energy matrix containing the imaginary η as the Büttiker probes contacts. The η is related to the scattering rate which covers, namely, acoustic phonons, polar optical phonons, and electron-electron interactions. The magnitude of the η can be corresponded to the scattering rates as mentioned in Ref. [19].
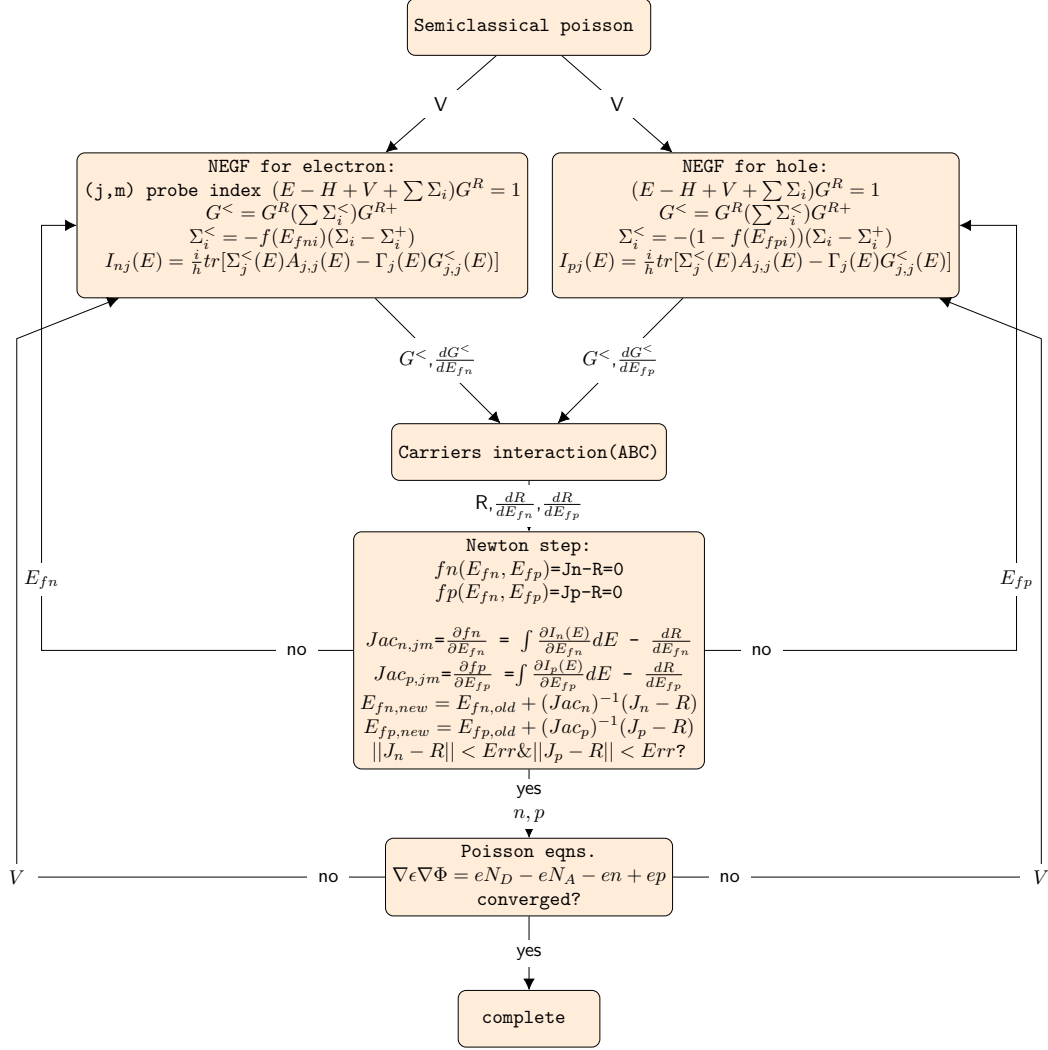
Fig. 4.5.: The BPRG program flowchart.

To prevent additional states created in the bandgap, the Σ^R is energy dependant, exponentially decaying in the band gap, to mimic the Urbach tail.

$$\Sigma_\eta^R(x, \boldsymbol{k}_{||}, E) = \begin{cases} \eta \cdot e^{-\frac{E_C(x, \boldsymbol{k}_{||}) - E}{\lambda}}, & \text{below conduction band} \\ \eta, & \text{above conduction band} \end{cases} \tag{4.25}$$

4.3.7 Impact of the off-diagonal Jacobian

Current conservation loop is solved iterative with Newton's method to find the probe Fermi levels for electrons and holes. Convergence can be quantified by the residual of Eq. (4.23).

By retaining the Jacobian off-diagonality, the convergence rate can be improved at the expense of more computation time and memory. The improvements are dependent on the type of structures and the electronic properties. InGaN effective simulation, Fig. 4.6 shows larger improvements for hole carriers due to their heavier mass.

off-diagonality	Time(secs)
0	65.2727
2	151.379
6	197.1
8	241.096
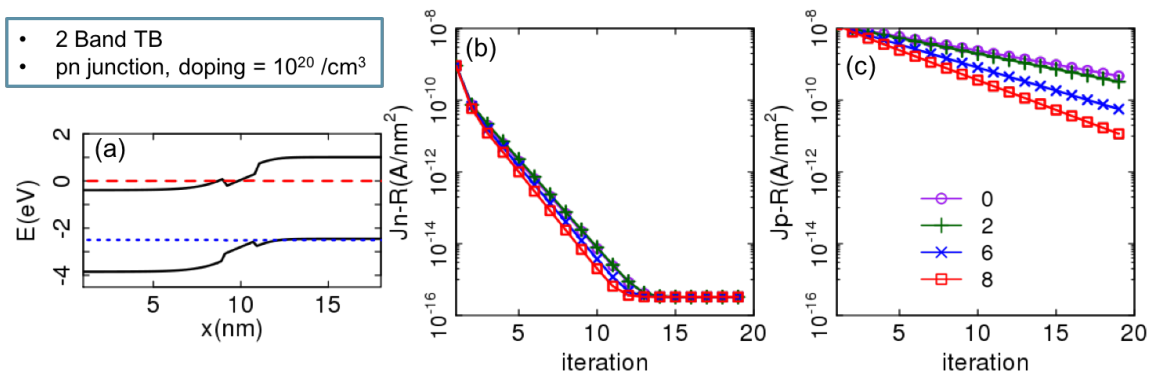
Fig. 4.6.: (a) Bandstructure of the device. For the current conservation loop, convergence rate of electron (b) and hole(c).

4.3.8 Contact self energy

In Eq. (4.6), Σ_S^R and Σ_D^R are the contact self-energy. Sancho-Rubio [97,98] method is used iteratively searching the surface green function. An η was in the original paper for the stability of the iterative scheme. Due to the device self energy, we have purposely matched the η such that a semi-infinite contact extending from the device can be achieved.

To demonstrate the importance, a position dependant density of states is plotted in the Fig.4.7. Having η matched contacts results in flat numerical DOS while the other result in confined and interfered wave pattern which is the oscillation increases as the η value increases.
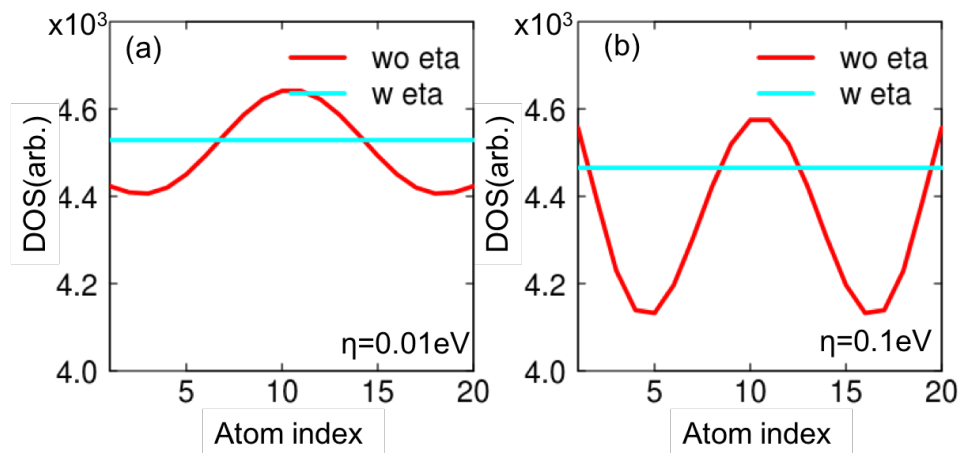
Fig. 4.7.: Density of states resolved at a single energy/k point shows the effect of η in the leads.

4.3.9 Scattering Self energy (η vs. Mobility)

With η mimicking the scattering, the carriers in the device can be scattered with energy loss travelling through a homogeneous doped material. The quantity of η can be further justified by matching experimentally observed mobility.

The transport calculation should be done with small bias, 10^{-2}eV, applied across the device with free carriers matching doping level by finding the correct potential by, e.g., solving Poisson equation. With $R(L) = V_{sd}/I(L)$, the resistance can be calculated for different device lengths as shown in Fig.4.8. The slope of R(L) can deduct the resistivity(ρ) as in Eqn.5.12. Mobility can be calculated by Eqn.4.27.

$$\rho = \frac{dR}{dL} \tag{4.26}$$

$$\rho = \frac{1}{q(\mu_n n + \mu_p p)} \tag{4.27}$$
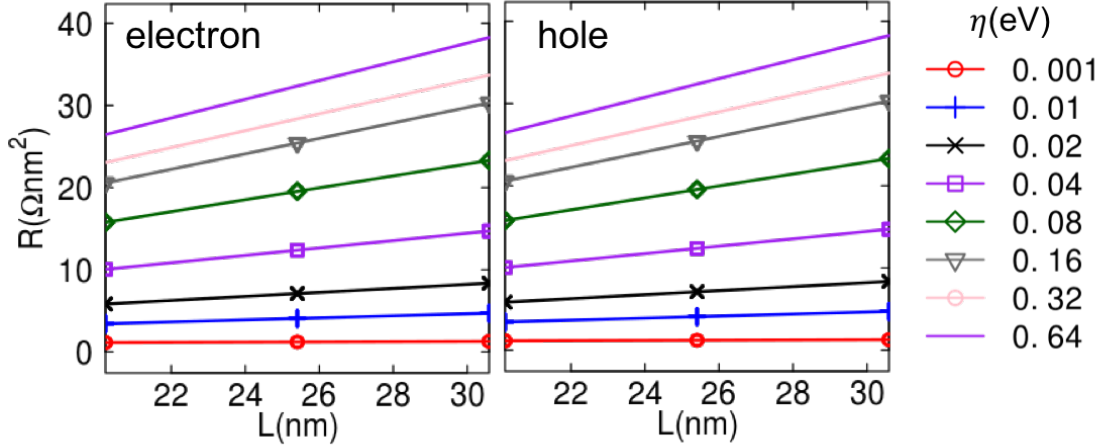
Fig. 4.8.: Resistance vs. homogeneous resistor length(L) is plotted for electron and holes with different scattering self-energy(η).

4.3.10 The importance of BPRG on NEGF calculation

IV curve is shown in Fig.4.9 in log and linear scale. Two types of currents exist, one is the recombination current which is the net current from the probes, the other one is the thermionic current flying over the barrier. A bias dependent balance between

thermionic and recombination current is demonstrated where $I_{total} = I_{recombined} + I_{thermionic}$.
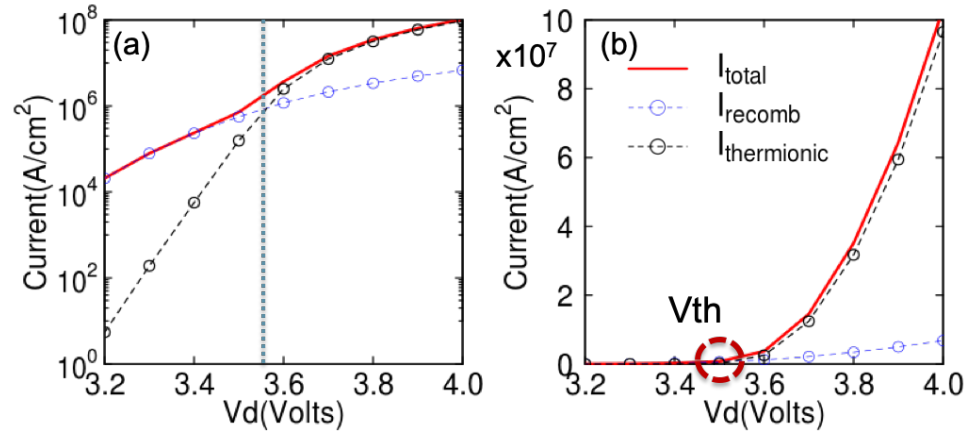
Fig. 4.9.: Current voltage characteristics of an pn diode in log(a) and linear (b) scale. Three kinds of current are represented with $I_{total} = I_{recomb} + I_{thermionic}$.

At low bias voltage, thermionic current is suppressed by a higher barrier and the total current is then mainly given by recombination (see Fig.4.9(a) and (b)). At high bias voltage, the recombination current increases due to increased carrier density in the quantum well. However, the effective barrier is much lower at higher voltages and the total current has an increasing thermionic contribution (see Figs. 4.9(c) and (d). The relevance of recombination is larger at lower voltages.
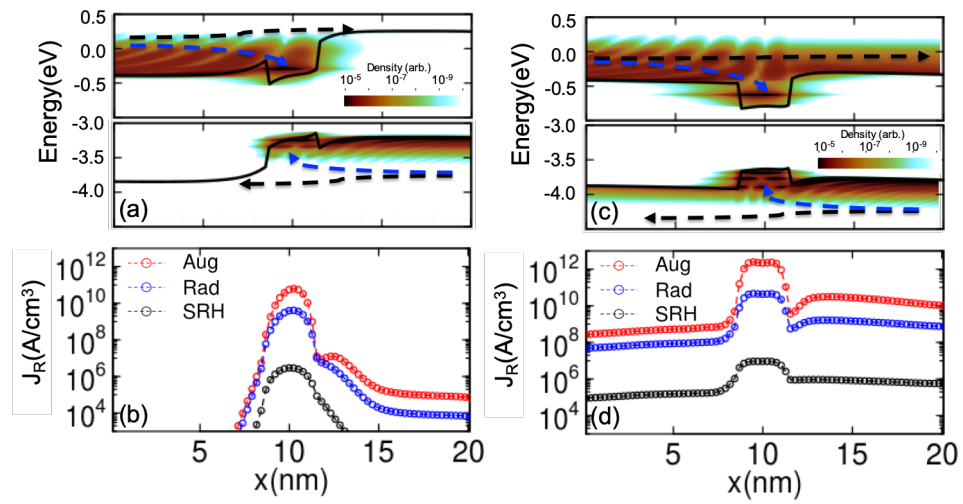
Fig. 4.10.: (a) Spatially resolved recombination current for the device described in the main text for different voltages. Conduction and valence bands (lines) and contour plot of the energy and position resolved carrier density 2.0V (b) and 4.0V (c). Arrows indicate recombination current (green) and thermionic current (red).

5. BPRG/DD COMPARISON ON III-NITRIDES OPTO-ELECTRONICS SIMULATION

5.1 Introduction

State-of-the-art semiconductor device fabrication techniques allow for device design at the atomistic length scale [99]. The performance of nanodevices is equally influenced by coherent quantum mechanical phenomena (such as confinement, tunneling and interference) [100, 101] and incoherent scattering of electrons on device imperfections and lattice vibrations [86, 102]. The performance of solar cells [103, 104], lasers [105] and light emitting diodes [2, 16] critically depend on the incoherent interaction of electrons with phonons and photons and the interplay between radiative, Auger and Shockley-Read-Hall (SRH) recombination. Carrier generation and recombination affect the off-current and switching characteristics of tunneling field effect transistors [106, 107]. The non-equilibrium Green's function method (NEGF) is among the most general methods to describe coherent and incoherent transport physics [102]. Due to the large numerical load when incoherent scattering is included in the self-consistent Born approximation [102], NEGF is typically applied in the coherent transport limit [95]. This is particularly problematic in nanodevices with pronounced incoherent effects [108].

There are various algorithms to include incoherent scattering in NEGF. The self-consistent Born approximation can rigorously treat incoherent scattering [102], carrier generation [109] and recombination [110]. However, the self-consistent Born approximation involves several nonlinear and highly dimensional integro-differential equations, which yield high computational load. The multi-scale and multi-physics NEGF implementation of Ref. 16 had been designed for modeling light emitting diodes with low numerical load. It requires full charge carrier thermalization in each quantum

well. Electron-hole recombination process is limited to the fully thermalized quantum wells as well. The Büttiker-probe model [88, 111, 112] represents a good compromise between the accuracy of NEGF and the numerical efficiency of heuristic scattering models for devices with incomplete carrier thermalization. In this work, the Büttiker-probes are extended to cover electron-hole recombination and generation in addition to its traditional application space of mobility limiting intraband scattering. Current conservation for intraband and interband scattering is ensured. NEGF predictions with the augmented Büttiker-probes are benchmarked against the drift-diffusion(DD) method of Atlas [113]. DD is at the core of industrial technology computer aided design (TCAD) tools for micro-scale devices [4, 114]. DD is known for its computational efficiency, but it requires to additional correction terms for mimicking coherent quantum effects [115–117]. The NEGF with Büttiker-probe transport predictions of pn-junctions agree quantitatively with DD results of the ON-current density and with results of the density in thermalized device regions. pn junctions that include quantum wells can serve as solar cells [118, 119] and photo-detectors [120]. Therefore, the new method is also benchmarked against a quantum corrected DD model for carrier recombination and light absorption. Deviations are found in cases with pronounced tunneling and interference effects. It is worth to mention the method is compatible with arbitrary basis representations, ranging from effective mass [121] and k.p [122] to atomistic approaches [123–126].

5.2   Methodology of BPRG and DD

The new Büttiker probes are benchmark against state-of-the-art TCAD methods on two devices - a GaN pn diode and a GaN pn diode including an intrinsic InGaN quantum well centered at the p-n interface. GaN electrons and holes are modeled each in effective mass assuming the isotropic masses $m_e = 0.2m^*$ and $m_h = 1.25m^*$ [127]. The position dependent electron and hole recombination and generation [81] rate

($R_{R/G}$) depends on the contributions of SRH, radiative recombination, Auger effect and light absorption

$$R_{R/G}(x)$$
$$= R_{SRH}(x) + R_{radiative}(x) + R_{Auger}(x) + R_G(x). \tag{5.1}$$

The SRH recombination rate is given by Ref. [81]

$$R_{SRH}(x)$$
$$= \frac{N_n(x)N_p(x) - n_{intrinsic}^2}{(N_n(x) + n_{intrinsic})/A + (N_p(x) + n_{intrinsic})/A} \tag{5.2}$$

with $A = 2.6 \times 10^6 s^{-1}$, the empirical parameter of the inverse recombination lifetime [114, 128, 129], $n_{intrinsic}$ the intrinsic carrier density [130] and $N_{n,p}$, the density of electrons (n) and holes (p). We solve the radiative recombination rate by [81]

$$R_{radiative}(x) = B \cdot N_n(x)N_p(x) \tag{5.3}$$

with the empirical parameter [114, 128, 129] $B = 1.48 \times 10^{-11} cm^3 s^{-1}$. We determine the Auger recombination rate with [81]

$$R_{Auger}(x) = C \cdot \left(N_n(x)^2 N_p(x) + N_p(x)^2 N_n(x)\right) \tag{5.4}$$

with the empirical parameter [114, 128, 129] $C = 1.6 \times 10^{-30} cm^6 s^{-1}$. Note that we use the same ABC parameters for all NEGF and TCAD results literature. In most calculations, the generation current density $R_G(x)$ is set to 0. Only when explicitly mentioned that illumination is included, the generation current density R_G in the well is determined by integrating photon numbers of the solar spectrum of energies larger than the bandgap of $In_{0.13}Ga_{0.87}N$. Outside the well, $R_G(x)$ is assumed to vanish

$$R_G(x) = \begin{cases} R_G, & x \in \text{InGaN} \\ 0, & \text{otherwise.} \end{cases} \tag{5.5}$$

The performance of the two devices is solved in NEGF with the new Büttiker probes. The NEGF results are benchmarked against DD and quantum corrected DD model (SILVACO-ATLAS [113]) results.

For all models, the spatially resolved recombination and generation rate $(R_{R/G}(x))$ is multiplied with the elementary charge and integrated along the total device to solve for the total recombination and recombination current density $J_{R/G}$.

$$J_{R/G} = \int_0^L R_{R/G}(x)dx. \tag{5.6}$$

For each carrier type a current conservation law modified by the recombination and generation is fulfilled

$$J_{s,n} + J_{d,n} + J_{R/G} = 0$$
$$J_{s,p} + J_{d,p} - J_{R/G} = 0. \tag{5.7}$$

$J_{s/d,n}$ $(J_{s/d,p})$ defines the source/drain current density for electrons (holes). The total measurable current density at the source is given as

$$J_{total} = J_s = J_{s,n} + J_{s,p}. \tag{5.8}$$

An equivalent equation holds for the drain current density.

5.2.1   NEGF with Büttiker probes

Electron and hole properties are solved within the NEGF method [87]. To limit the computational load, the devices are partitioned and Green's functions are solved recursively on the resulting slabs [96]. The retarded Green's function G^R is solved by the Dyson equation [87]

$$G^R = [E - H - \Sigma_S^R - \Sigma_D^R - \Sigma_{BP}^R]^{-1}. \tag{5.9}$$

The lesser Green's function $G^<$ is given in the Keldysh equation

$$G^< = G^R(\Sigma_S^< + \Sigma_D^< + \Sigma_{BP}^<)G^{R\dagger}. \tag{5.10}$$

All Green's functions and self-energies are matrices in the discretized positions space. Their dependency on the in-plane momentum $k_\parallel$ and energy E is omitted in Eqs. (5.9) and (5.10) for better readability. The source and drain contact self-energies are given

by $\Sigma_S^{R,<}$ and $\Sigma_D^{R,<}$. Scattering of electrons and holes is included with Büttiker probe self-energies $(\Sigma_{BP}^{R,<})$ [90, 93, 96]. Quantities such as the density of states, the particle density, the state occupancy and the current density can be deduced from the Green's functions as typical for the NEGF method [87, 131].

The retarded Büttiker probe combines all intra-band scattering processes, such as scattering on various phonons, impurities and electron-electron scattering into the empirical scattering parameter η [16]. To resemble the Urbach tail [132, 133] in GaN, η is exponentially decaying into the band gap. For electrons in the conduction band, the retarded Büttiker probe self-energy reads

$$\Sigma_{BP,n/p}^R(x, x', k_\parallel, E) = \delta(x - x')$$

$$\times \begin{cases} a\eta_n, & \text{if } E \geq E_c\left(x, k_\parallel\right) \\ a\eta_n \cdot \exp\left(-\frac{E_c(x,k_\parallel)-E}{\lambda}\right), & \text{if } E_c\left(x, k_\parallel\right) > E \geq \frac{E_c+E_v}{2} \\ a\eta_p \cdot \exp\left(\frac{E_v(x,k_\parallel)-E}{\lambda}\right), & \text{if } \frac{E_c+E_v}{2} > E \geq E_v\left(x, k_\parallel\right) \\ a\eta_p, & \text{if } E_v\left(x, k_\parallel\right) > E. \end{cases} \quad (5.11)$$

In all NEGF calculations, the mesh size a is set to 0.259 nm.

The retarded Büttiker probe for holes in the valence band has the same formula, but with valence band parameters. Similar to Ref. 45, the electron and hole mobility are deduced from the respective resistivity of n- or p-doped homogeneous material samples solved with NEGF and Büttiker probes

$$\rho_{n,p} = \frac{dR_{n,p}^\Omega}{dL} = \frac{1}{q(\tilde{\mu}_{n,p}N_{n,p})}. \quad (5.12)$$

Here, R^Ω refers to the resistance of GaN samples of length L, $R^\Omega(L) = V_{sd}/I(L)$. The applied Fermi level difference of source and drain in the mobility calculation is set to 10 meV. $I(L)$ is the length dependent current density for electrons or holes and solved for $L = 20$ nm and $L = 25$ nm. The empirical scattering parameter $\eta_n = 0.05$ eV for electrons and $\eta_p = 0.06$ eV holes are chosen such that the respective NEGF predicted mobility agrees with $\tilde{\mu}_e = 56.88 cm^2/(Vs)$ and $\tilde{\mu}_h = 10.0 cm^2/(Vs)$ (taken from Ref. 134). For completeness, Fig.5.1 shows the GaN hole and electron

mobility as a function of the respective η. The band tail parameter λ is chosen to be 55 meV for electrons according to Ref. 135. The same value is assumed for holes.
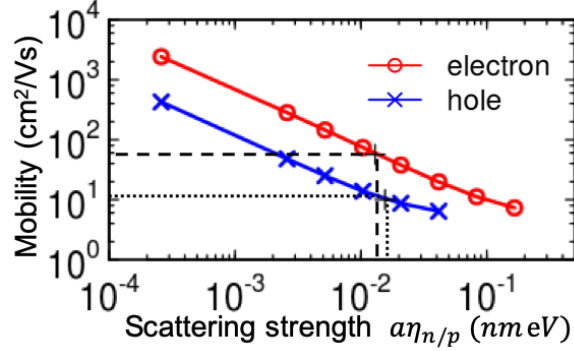
Fig. 5.1.: NEGF predicted mobility of a homogeneous semiconductor with p and n doping density of $10^{20}/cm^3$ as a function of the product of $\eta_{n,p}$ of Eq. (5.11) with the mesh spacing a.

The "lesser than" Büttiker probe self-energy $\Sigma_{BP}^<$ is depending on the Büttiker probe Fermi-levels, $\mu_{n/p}(x)$

$$\Sigma_{BP,n/p}^<(x, x', k_\parallel, E) =$$
$$\begin{cases} -F\left(\mu_n(x), E\right)\left(\Sigma_R(x, x', k_\parallel, E) - \Sigma_R^\dagger(x, x', k_\parallel, E)\right), \\ \quad \text{if } E \geq \frac{E_c + E_v}{2} \\ -(1 - F\left(\mu_p(x), E\right)\left(\Sigma_R(x, x', k_\parallel, E) - \Sigma_R^\dagger(x, x', k_\parallel, E)\right), \\ \quad \text{if } E < \frac{E_c + E_v}{2}. \end{cases} \quad (5.13)$$

Here, F is the equilibrium Fermi distribution function. In this work, $\mu_n(x)$ and $\mu_p(x)$ are solved iteratively to satisfy the overall current conservation

$$R_n(x) = R_p(x) = R_{R/G}(x) \quad (5.14)$$

R_n and R_p represent the net electron and hole current of the Büttiker probe at position x, respectively. In the state-of-the-art Büttiker probe models, $\mu_n(x)$ and $\mu_p(x)$ are solved separately which ensures both, electron and hole current conservation

individually. Equation (5.14) agrees with the common Büttiker probe model for the case of $R_{R/G} = 0$.

The retarded source and drain self-energies $\Sigma_{S,D}^R$ are solved iteratively following Ref. [97, 98]. To guarantee smooth electron and hole transitions at the device/source and device/drain interfaces, the retarded Büttiker probe self-energy of Eq. (5.11) is included in the source and drain self-energy calculation [89, 136]. The Büttiker probe and NEGF equations are iterated with the Poisson equation to achieve charge self-consistency. Piezoelectric and spontaneous polarizations are included as well following Ref. 16.

5.2.2 Drift diffusion models

The purely semiclassical bulk drift-diffusion(DD) model [137] is applied on the homojunction pn diode with a mesh spacing of 0.1 nm. In case of the pn diode including a quantum well, the DD model is augmented with quantum corrections for the bound states (DD+qwell) in the well region [113]. That heterojunction device is discretized with an adaptive real space mesh [113] with average mesh spacing of 0.16 nm. Depending on their energy and location, electrons and holes are separated into two groups, "bound states" and "bulk states". For electronic energies below the barrier potentials ("bound states") at the GaN/InGaN interfaces, the Schrödinger equation is solved assuming the wave functions vanishing at the Schrödinger domain boundaries (i.e. Dirichlet boundary conditions). The solution domain of the Schrödinger equation is exceeding the InGaN quantum well by 10 nm in both directions to account for the wavefunction penetration into the barriers. Artificial bound states in GaN that would arise from the Dirichlet boundary conditions are avoided by limiting the lower bound of the GaN band edge to the barrier potential at the GaN/InGaN interfaces [113]. For "bulk states", the DD equations are solved throughout the structure, but the InGaN band edge is shifted to the minimum of the barrier potentials at

the unaltered GaN/InGaN interfaces [113,138]. This ensures all "bulk states" do not face quantum well potential confinement.

Charge carriers of the two energy sets ("bound" and "bulk"), are coupled to each other by a capture-escape model [113]. Capture-escape rates for electrons and holes respectively are added to the DD continuity equations to allow transitions between "bound" and "bulk" particle groups [113]. Recombination-generation mechanisms are included in the continuity equations as well (Eqs. (5.2-5.4)). Detailed balance is ensured and all Fermi levels uniquely determined by using the same rates for carrier gain/loss in the "bound" and "bulk" groups and for generation and recombination, respectively. For charge self-consistency, the sum of the electron and hole "bound" and "bulk" density is iterated with the Poisson equation.

A summary of the models described is shown in Fig. 5.2.
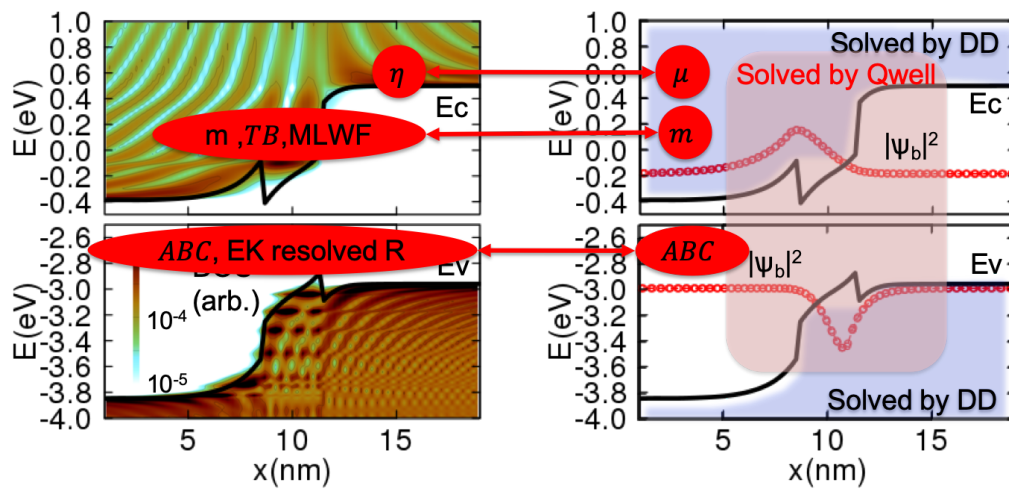
Fig. 5.2.: Summary of the two models described, DD and BPRG with their corresponding parameters.

5.3 BPRG vs. Drift-Diffusion with pn-diodes

Three application scenarios (a pn-diode, a pn-diode with a quantum well and an illuminated pn-diode with quantum well) are used to benchmark the Büttiker probe model against the semiclassical and quantum corrected semiclassical models. The comparison shows the two methods agree very well in situations without pronounced quantum effects. The quantum corrections of the semiclassical model capture quantum effects but the results still deviate from those of a pure quantum mechanical treatment.

The pn diode is composed of 10 nm p type and 10 nm n type doped GaN with the doping concentration of $10^{20}/cm^3$ in each region. Both regions are periodic in the transverse directions. The pn diode with the quantum well differs from the pn diode by a 3.0 nm thick intrinsic $In_{0.13}Ga_{0.87}N$ quantum well layer. If not explicitly mentioned otherwise, the temperature is assumed to be 350 K.

5.3.1 GaN pn junction

Figure 5.3(a) shows the position resolved band edge of the GaN pn diode solved in DD and NEGF. Both results agree quantitatively. The charge distributions of the two methods are depicted in Fig. 5.3(b). The majority carrier in each region shows agreement between the two models while the minority charge from NEGF is around 10^3 and 10^5 times higher in the depletion region for electrons and hole, respectively. The minority carriers enter the oppositely doped area due to tunneling - as illustrated by the contour plot of the energy resolved carrier density of NEGF in Fig. 5.3(a). Note, the tunneling is longer ranged for conduction band states with their lighter effective mass than for the states in the valence band. DD-based models do not capture this tunneling effect and the state-of-the-art quantum corrections do not apply to "bulk states". The energy resolved density also illustrates Urbach tails with the additional density at energies below (above) the conduction (valence) band edge.

It is worth to mention, decreasing λ to 5 meV in Eq. (5.11) reduced the Urbach tail and decreases the OFF-current by 10% while the ON-current changes only marginally.
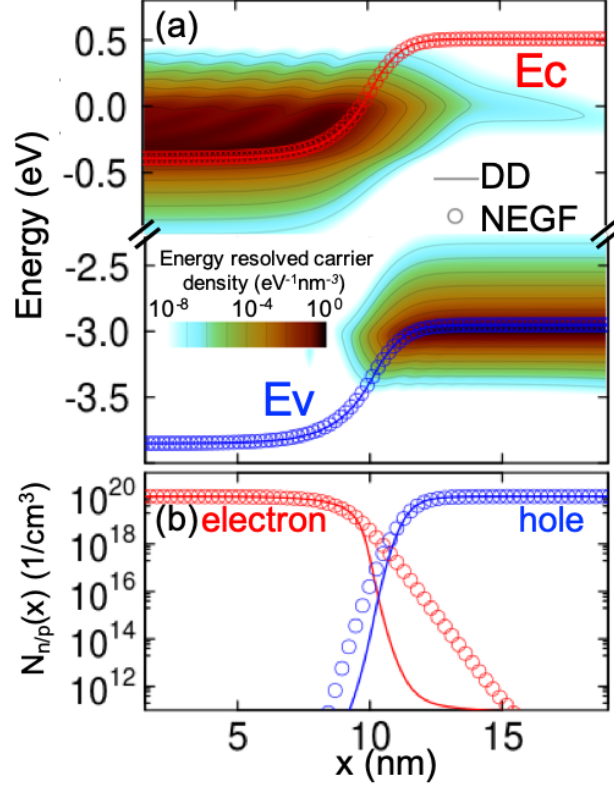
Fig. 5.3.: The GaN pn diode described in the main text with a voltage of $V_{sd} = 3.0V$ applied. (a) Conduction and valence band profiles solved in DD (lines) and NEGF with Büttiker probes (symbols) along with contour plots of the energy resolved carrier densities at vanishing in-plane momentum. (b) Position resolved electron and hole densities solved in DD (lines) and NEGF with Büttiker probes (symbols).

Differences in the density entail deviations of the recombination current density of the two models (see Eqs. (5.2)-(5.4)). This is illustrated in Fig. 5.4 (a) which shows the various contributions to the position resolved recombination rate of DD and NEGF with Büttiker probes for the situation in Fig. 5.3(b). For higher applied bias, the effective barrier between n- and p-doped region reduces. Minority carrier

tunneling becomes less relevant compared to the thermionic emission current [139]. In consequence, the densities of DD and NEGF with Büttiker probes at a higher voltages agree better and so do the recombination rate contributions in Fig. 5.4(b).
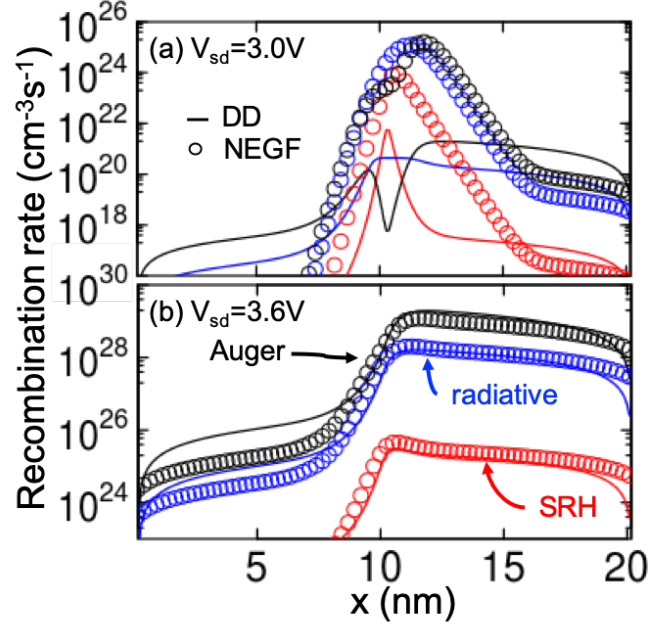
Fig. 5.4.: Spatially resolved recombination rates ($R_{SRH}(x)$, $R_{radiative}(x)$ and $R_{Auger}(x)$) for the pn diode of Fig. 5.3 solved in NEGF with Büttiker probes (symbols) and DD (lines) for applied voltages of V_{sd}=3.0 V (a) and 3.6 V (b).

The comparison of the total current density (Eq. (5.8)) predicted with DD and NEGF with Büttiker probes follows the same trend as can be seen in Fig.5.5. Low voltages show pronounced deviations, whereas voltages above about 3.2 V yield quantitive agreement in the total current density. The recombination current density deviates until about 3.5 V, but its relative contribution is insignificant for voltages above 3.2 V. Note that the slope of the IV-curve below V_{sd} =3.4V differs significantly between the two models due to the different treatment of tunneling.
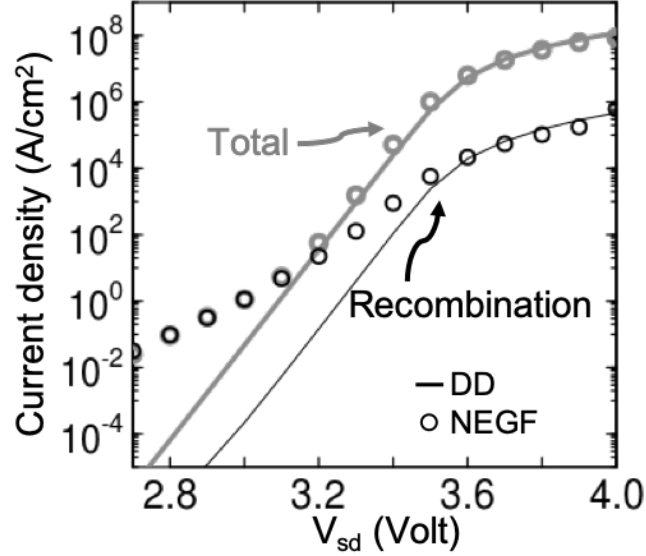
Fig. 5.5.: Current-voltage characteristics of the pn diode of Fig. 5.3 predicted by NEGF with Büttiker probes (symbols) and DD (lines). The total current density (gray) contains the contributions from the recombination current density (black).

5.3.2 InGaN quantum well embedded in GaN pn junction

When an $In_{0.13}Ga_{0.87}N$ layer is added to the center of the GaN pn junction, a quantum well in the conduction and valence band forms (see Fig. 5.6(a)). Unaltered DD density results follow the band profiles [137]. Consequently, the unaltered DD calculations yield maxima in the carrier density close to the $In_{0.13}Ga_{0.87}N$/GaN interfaces (see Fig. 5.6(b)). In contrast, quantum corrected calculations cover quantum confinement effects with wavefunction maxima of "bound states" closer to the quantum well center (see dashed lines for conduction $\Psi_{n,qwell}$ and valence $\Psi_{p,qwell}$ band "bound states" in Fig. 5.6(a)).

Calculations of NEGF with Büttiker probes do not distinguish between confined and continuum states but allow for smooth transitions between them. This is illustrated with the contour plot of the energy and position resolved density of states (DOS) in Fig. 5.6(a).

Confined carriers in the quantum well extend into the continuum of states. Continuum states are also modified by the interference effects at the quantum well boundaries. Higher order quantum well states with energies well beyond the barrier heights are still visible in the DOS continuum (yellow lines in Fig. 5.6(a)). These effects are missed in the quantum corrected DD model (DD+qwell) that separates "bound" and "continuum" spectra. In detail, the conduction and valence band ground state energies predicted in NEGF are approximately 0.13 eV higher than in DD+qwell. In consequence, the local density of the three models differ (see Fig. 5.6(b)).

For an applied voltage of V_{sd}=4.0V the quantum well ground states of conduction and valence bands are well confined (see Fig. 5.7). In this case, a distinction of "bound" and "continuum" states as done in DD+qwell is obvious. However, the energy resolved density in Fig. 5.7 for energies above the barrier potential (i.e. "continuum" states) still shows significant interference due to the potential change at the quantum well. The interference pattern of the electron (hole) density are best visible in the n-doped (p-doped) region. These quantum effects add resistance to the Büttiker probe scattering. Since the Büttiker probe scattering strength was tuned to match the mobility assumed in the DD calculations, the total current density of the device in Fig. 5.7 is predicted lower in NEGF than DD. This is illustrated in Fig. 5.8 which shows the total ON current is about two times smaller in NEGF than DD. Since the density of the confined state in the quantum well of NEGF calculations is smaller than in DD (see Fig. 5.6b), the recombination current density of NEGF is smaller than in DD, too (see black lines and symbols Fig. 5.8).

5.3.3 Illuminated InGaN quantum well embedded in GaN pn junction

When various carrier generation rates due to solar light absorption are included in the calculations of the InGaN quantum well system of Figs. (5.6)-(5.8), the predicted current density is linearly shifted to negative values (see Fig. 5.9) as common for solar cell operations [140]. The open circuit voltage for DD calculations at 350 K
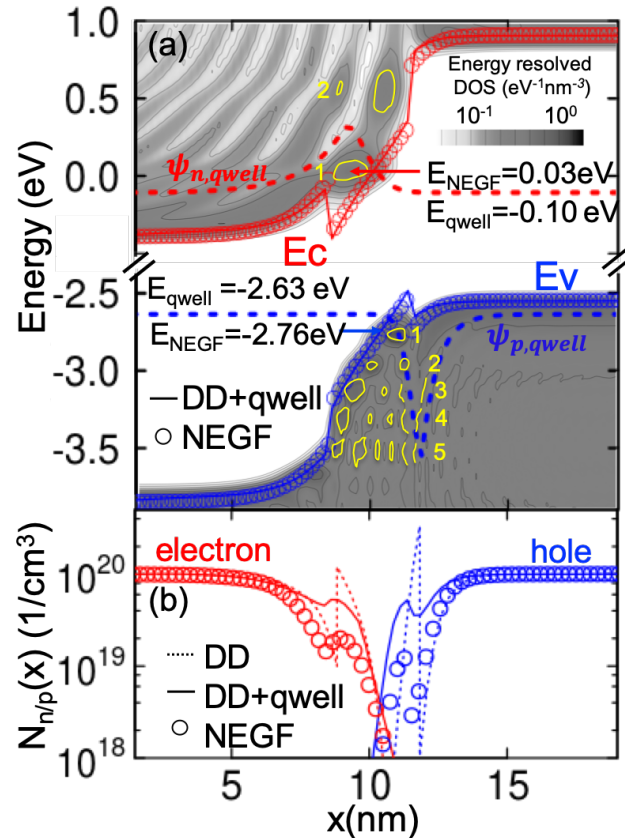
Fig. 5.6.: The GaN pn diode with an InGaN quantum well described in the main text for an applied voltage of $V_{sd} = 2.6V$. (a) Conduction and valence band profiles solved in DD+qwell (lines) and NEGF with Büttiker probes (symbols) along with a contour plot of the energy resolved density of states at vanishing in-plane momentum. The dashed lines show the squared absolute value of the "bound" quantum well wave functions in the DD+qwell model. For reasons discussed in the main text, the ground state energies of DD+qwell and NEGF differ, and NEGF covers quasi-bound states in addition (indicated with yellow lines and labeled with numbers). (b) Position resolved electron and hole densities solved in DD+qwell (lines) and NEGF with Büttiker probes (symbols).

temperature is smaller than in the NEGF case. This is a result of the different quantum well densities and recombination rates discussed already in Figs. 5.6(b) and
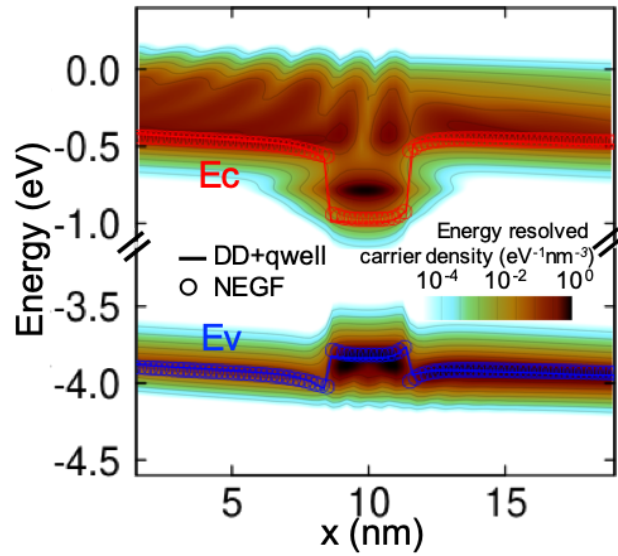
Fig. 5.7.: The GaN pn diode with an InGaN quantum well of Fig. 5.6 with a voltage of $V_{sd} = 4.0V$ applied. Conduction and valence band profiles solved in DD+qwell (lines) and NEGF with Büttiker probes (symbols) are shown along with a contour plot of the energy resolved density of states at vanishing in-plane momentum solved in NEGF with Büttiker probes.

5.8. With a lower temperature of 100 K, the ground state energy of the quantum well turns out to be larger than the confinement potential and the DD model does not find any "bound states". Then, the quantum well density of DD calculations is lower than in NEGF, and same holds for the recombination current density. Therefore, at 100 K, a higher open circuit voltage is observed in DD than in NEGF.

5.4 Utilize Different Basis

With basis of more atomic orbitals, higher energy bands can be captured in the bandstructure along with non-parabolic feature included and therefore provide more realistic simulation results. For a pn diode with single quantum well structure, 20
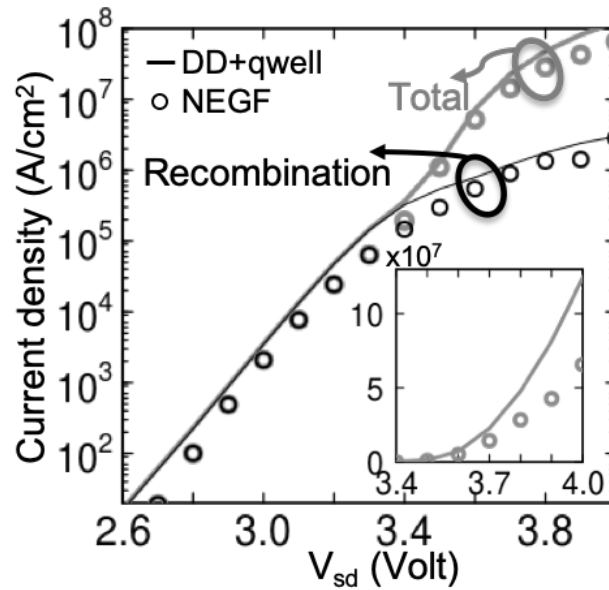
Fig. 5.8.: Current-voltage characteristics of the GaN pn diode with a InGaN quantum well of Fig. 5.6 predicted by NEGF with Büttiker probes (symbols) and DD+qwell (lines). The total current density (gray) contains the contributions from the recombination current density (black). The inset illustrates a difference of approximately 2x in the ON-current predicted with NEGF and DD.

bands(sp3d5s* with spin) tight-binding model and 2 band model are used for comparison.

Current voltage relationship is shown in Fig.5.10. TB results is shown to be higher in both total and recombination currents. Fig. 5.11 provides the spatially resolved band structure, recombination current, and carrier density for the two basis. Due to the atomic resolved probe, Ga and N atoms are of different slabs. N atoms have more carrier density while Ga atoms less as can be observed in the fluctuation of Fig. 5.11(c). Carrier density tunnels more into the barrier as predicted by the TB partially due to the flattened quantum well as in Fig. 5.11(a). Through the ABC eqautions, the probe recombination current is predicted differently as in Fig. 5.11(b) with more recombination occurs on the left interface of the QW with high manitudes.
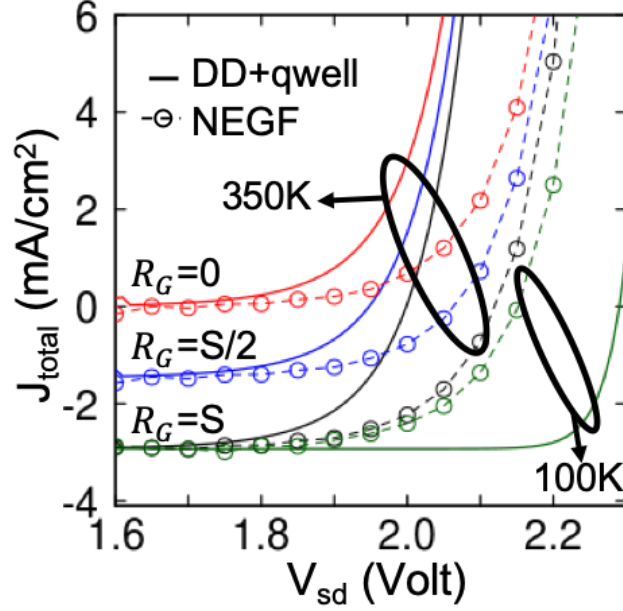
Fig. 5.9.: Current-voltage characteristics of the GaN pn diode with a InGaN quantum well of Fig. 5.6 predicted by NEGF with Büttiker probes (symbols) and DD+qwell (lines) with a finite electron-hole generation rate of S= $6.4 \times 10^{22} cm^{-3}s^{-1}$ in the quantum well. The different quantum mechanical treatment of the bound and quasi-bound states of the two methods leads to differences in the open-circuit voltage at 350 K and 100 K as detailed in the main text.

To be noted, the Σ^R in this section is not tuned to match the experimental mobility as done in Fig. 5.1

5.5   Conclusion

This work augmented the Büttiker probe based scattering model in the nonequilibrium Green's function framework to efficiently model electron-hole recombination and generation processes. Electrons and holes are modeled as separate particles that observe particle continuity equations with explicit particle creation and destruction rates. The combined system of holes and electrons conserves the current. These
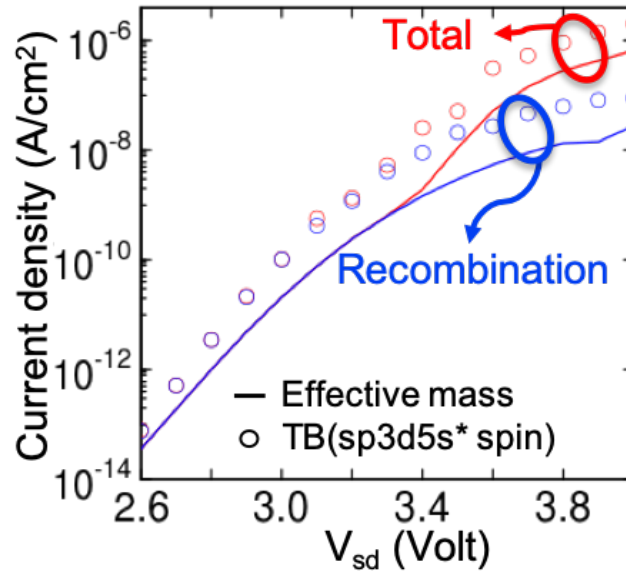
Fig. 5.10.: Current-voltage characteristics of the pn diode with a quantum well of Fig. 5.6 predicted by NEGF with Büttiker probes (symbols) and DD+qwell (lines). The total current density (gray) contains the contributions from the recombination current density (black).

Büttiker probes are applied on transport of electrons and holes in GaN pn-junctions with and without an embedded InGaN quantum well. The results are benchmarked against Drift-Diffusion and quantum-corrected Drift-Diffusion calculations of Silvaco's TCAD tool Atlas [113]. The two methods agree quantitatively except for situations with pronounced carrier tunneling and interference. In particular, interference effects in the band continuum can create quasi-bound states that impact the optoelectronic device performance. In consequence and depending on the detailed device geometry, temperature and applied bias the open-circuit voltage of quantum well pn-junctions is underestimated or overestimated in state-of-art TCAD simulations.
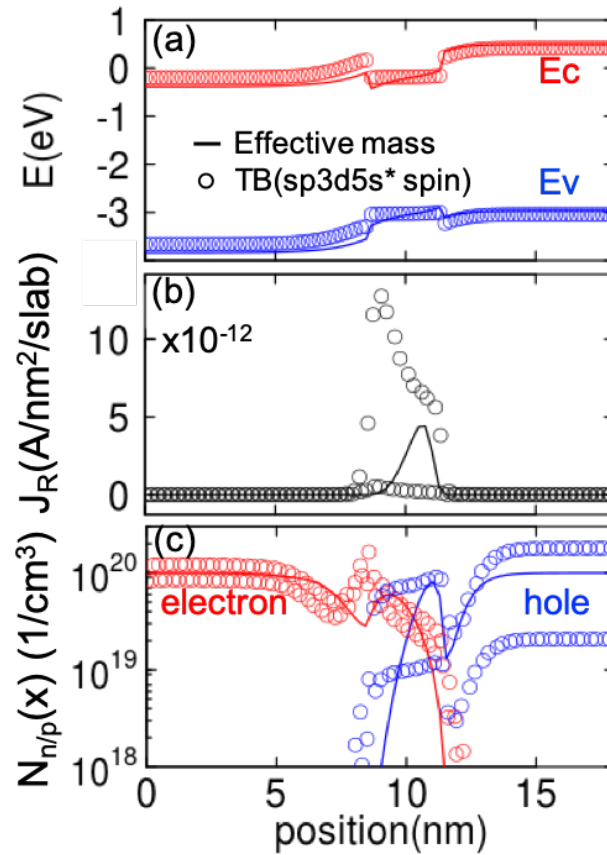
Fig. 5.11.: pn diode with a quantum well is biased at V_{sd}=3.0V. (a) Conduction bands and valence band are compared between the effective mass model(line) and 20 band tight-binding basis(symbol). (b)Slab resolved recombination current are compared between the effective mass model(line) and 20 band tight-binding basis(symbol). (c)Spatially resolved carrier density of electron(red) and hole(blue) are compared between the effective mass model(line) and 20 band tight-binding basis(symbol).

6. ANTI-AMBIPOLAR FROM BP MOS$_2$ 2D INTERFACIAL DEVICE

6.1 2D pn junction

pn junction is the basic building block for all semiconductor applications, e.g. solar cell, LED [4], transistors, logic gates,etc., and has been thoroughly studied as textbook example. With the emergence of 2D materials, new device architectures, characteristics and applications have been inspired and require further studies. Materials of complete opposite characteristics can be combined as atomic Lego [8] while p and n types can be combined to form atomic 2D pn junctions [9] anticipating the potential for transparent, flexible, high-efficiency electronic and optoelectronic applications. Different morphologies have been shown, planar 2D pn junction [141, 142] is shown to have longer depletion width [10] to reduce Fermi level pinning. Vertical junction [11, 12, 143] has been shown to demonstrate gate tunability affecting both doped areas and anti-ambipolar characteristics.

The anti-ambipolar(AAP) characteristic has been observed for some vertical p-n junctions [27, 144, 145] and is relevant for electronic applications as frequency doubler and phase shift keying circuits [145, 146]. AAP has two off-states for either positive or negative gate biases and an on-state in between with on-off ratio as large as 10^4. The materials range from 2D to 1D and from organic to crystalline. Experimental observation [9, 11, 144, 147–149] claimed it still a mystery [11] while some claimed to provide explanation only with semiclassical methods [145, 150] however most missing atomistic resolution with bandstructure explanation. AAP in BP/MoS$_2$ system has been of great interest. It's been shown to have strong interlayer recombination [151]. The responsivity to light has been measured to have potential opto-electronics applications. In the TCAD tool [9], drift-diffusion is used with effective mass approximation

for the lateral direction with measured mobility. For the vertical direction, mobility is approximated with hopping rate due to the Van der Waals inter-layer coupling. Pronounced quantum mechanical effects are expected due to ultra-thin device size and motivate for a thorough study on this system.

In this work, atomistic simulation is achieved with basis generated by density functional theory relaxed structure via maximally localized Wannier function [123]. With non-equilibrium Green's function, quantum transport with semi-infinite leads are conducted. Furthermore, with the expanded Büttiker probe method [152, 153] conventionally for carrier thermalization, inter-facial carrier recombination is further addressed along with electron/hole current conservation. The origin and criteria for AAP effect are provided and assessed.

6.2 Experiment vs. simulation setup for BP/MoS2 interface

The experimental device structure, fabrication, and characterization have been previously reported [145]. Briefly, self-aligned contacts with controlled dielectric extensions were patterned and deposited on isolated flakes of monolayer MoS_2 grown by chemical vapor deposition on doped Si substrates with 300 nm SiO_2. Mechanically exfoliated black phosphorus flakes were dry transferred onto the MoS_2, overlapping the self-aligned contacts. Electrodes for the black phosphorus were then patterned directly on top of the self-aligned contacts. The top gate dielectric and metal contacts were patterned and deposited in the same step to cover the semi-vertical p-n heterojunction. Electrical measurements were performed under vacuum at room temperature. The devices show anti-ambipolar (Gaussian) characteristics with top-gate bias sweeps where the peak position and heights can be further controlled by the bottom gate biases (Fig. 6.1(a)).

To simulate with atomistic method with feasible computation requirement, a scaling of the device is needed as done in Fig.6.1. Several differences deviate from the real experimental structure. First, only mono-layer BP and MoS_2 are simulated. Second,

length scales are reduced, e.g., the overlapped region is reduced to L nm, where L = 6, 10, 14 nm. Third, the contacts are approximated by highly doped BP/MoS_2 of $10^{20} cm^{-3}$. Fourth, the geometry is different where it becomes a fully lateral transport structure. V_{TG} and V_{BG} are applied on top gate and bottom gate, respectively, with the V_{SD} biased at 0.6V.
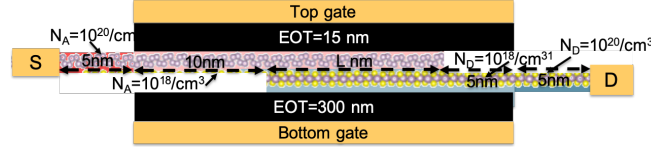
Fig. 6.1.: A simplified device is constructed to assimilate the experimental setup for NEGF calculation. Black phosphorus(upper) and MoS_2(lower) layers are overlapped and sandwiched between dielectrics of effective oxide thickness as indicated. Doping densities are assumed for each region. The top gate and the lower gate are attached to the dielectric.

The MoS_2/BP interface constructed as in Ref. [154] was studied by first principle calculations carried out by density functional theory (DFT), using projector-argument waves (PAWs) as implemented in the VASP code. In these calculations, the generalized-gradient approximation (GGA) with the Perdew-Burke-Ernzerhof (PBE) exchange-correlation functional was used with an energy cut-off of 500eV with a convergence criterion of 10^{-8} eV. The supercell was relaxed with an (8x8x1) Monkhorst-Pack grid. Additionally the Van der Waals correction was included by the semi-classical method DFT-D2) as implemented in VASP. The structure was relaxed until a force lower than 0.01 eV/A per atom was achieved.

Wannier90 [58] is used with Gaussian charge distribution on finite element cells [123]. Projection unto atomic basis is used for the initialization of the unitary matrix. For Mo atoms, d orbitals are used. For P and S atoms, hybrid orbitals sp3 is used. Disentanglement method is used to select bands and minimize spreading. MLWF basis is produced and read in with NEMO5 to map unto the device in Fig.6.1.

MLWF Hamiltonian from BP/MoS$_2$ interface is mapped unto the device. Recursive Green's function is used such that the device is partitioned into slabs laterally each attached with a Büttiker-probe. For Σ_R, constant $\eta = -i0.01eV$ are added diagonally above band edge and decay exponential in the band gap [16]. For each slab, Eqn.6.1 is satisfied with B and s being the Langevin recombination parameters [151]. $J_{n,j}(J_{p,j})$ is the electron (hole) current out of the j'th Büttiker-probe. $n_j(p_j)$ is the average electron (hole) density of the j'th slab. Due to inconsistency in unit [151], here we use s=1 and B=$6 \times 10^{-11}cm^{-3}s^{-1}$ equivalent to carrier lifetime of 1ns. The device operates in forward bias with V$_S$=0 and V$_D$ = 0.6eV. For the two sides, a highly doped region is assumed to mimic metallic contacts.

$$J_{n,j} = J_{p,j} = Bn_jp_j^s \tag{6.1}$$

6.3 AAP explaination

Bandstructure are plotted and compared between DFT and the MLWF basis for BP/MoS2 interface as in Fig.6.2(a). Extracting the MLWF basis generated from BP/MoS$_2$ interface for monolayer BP and MoS2, bandstructure is produced in Fig.6.2(b) and (c) compared against the DFT result. MLWF is shown to be transferable from a combined system to individual systems. This provide justification for the whole device in Fig. 6.1 using the same MLWF basis for monolayer or bilayer regions.

The current and voltage characteristics measured from experiment device is shown in Fig.6.5(a) with different combination of V_{BG} and V_{TG}. Simulation results are plotted in Fig.6.5(b) for simplified device Fig.6.1 demonstrating the same trend. First, increasing V_{BG} increases the AAP amplitudes. Second, increasing V_{BG} shifts the peaks of AAP toward lower V_{TG}. The origin of the AAP can be further understood as a serial connection of a nFET and a pFET as in Fig. 6.3(a). Fig.6.4(a)(b)(c) depicts a pFET with holes injected from the left with the barrier height increasing with
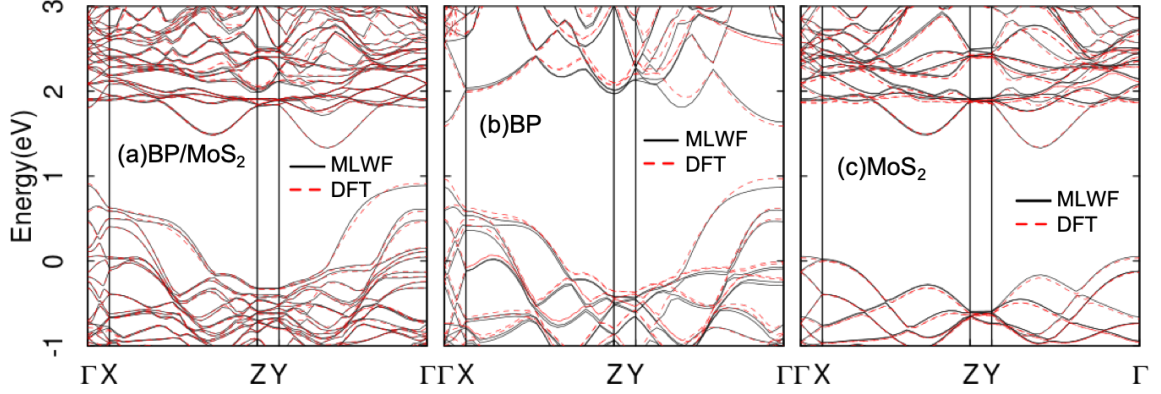
Fig. 6.2.: Bandstructure for (a)BP/MoS$_2$ bilayer system, (b)BP monolayer and (c)MoS$_2$ monolayer are generated with MLWF Hamiltonian and compared against DFT result. MLWF basis for (b) and (c) is extracted from the BP/MoS$_2$ bilayer system.

increasing V_{TG}. Fig.6.4(d)(e)(f) depicts a nFET with electron injected from the right with a barrier height increased with decreasing V_{TG}. Schematic is provided for the device in Fig. 6.3.

Conditions for AAP is summarized in the following:

1. type II junction is needed as in Fig.6.3(c) where minority carrier current density is screened at the nFET/pFET's on state.

2. Gate is required to induce barrier for turning off p and n FET respectively.

3. Recombination mechanisms in the overlap region, likely SRH or Langevin processes, is critical to ensure the on current of the AAP curve.

The experiment structure has micro-meters length of the overlapped region. It is tested here by altering the L for 6, 10 and 14 nm. As the overlapped region increases, the amplitude of the AAP is higher with a smaller bandwidth as in Fig. 6.6(a). Due to the uncertainty of the Langevin constant, B is altered and shows a trends of increasing amplitude with increasing rate as in Fig. 6.6(a).
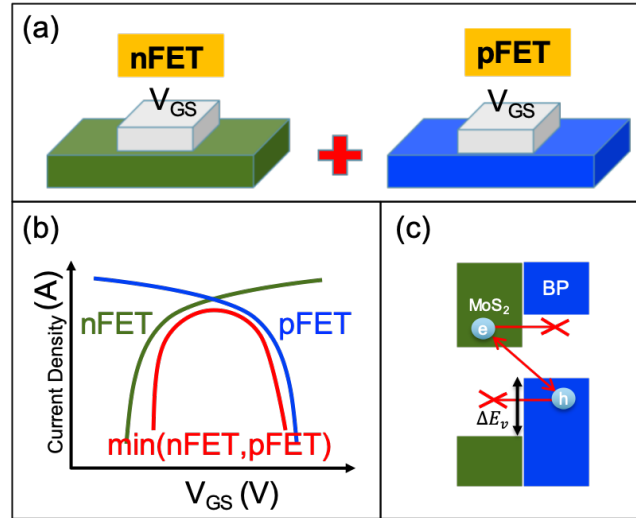
Fig. 6.3.: (a) The AAP device is composed of a nFET and a pFET with the interface serving as the "+" sign. (in series) (b) The IV curve for nFET and pFET. Depending on the interface carrier transport mechanism, different resulting IV curve should be observed. (c) Three types of transport mechanism can occur at the interface. Due to the type II heterojunction, direct tunneling is not possible. But electron and hole recombination is possible due to SRH, Langevin.

6.4 Conclusion

The principle of AAP characteristics observed in 2D pn junction is re-examined in this work with NEGF with recombination processes in the MLWF basis. With quantum transport, the off-current is confirmed to be turned off with type II band-alignment. Further with the expanded Bütiker probe mode, the device can be turned on with Langevin recombination at the 2D interface.
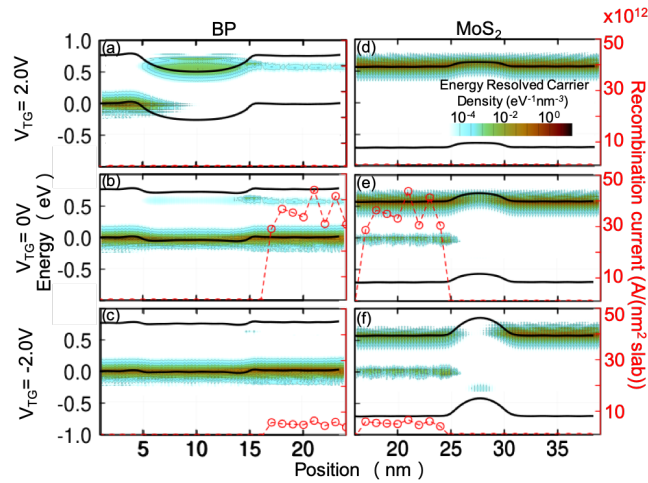
Fig. 6.4.: At V_{BG}=0, V_{TG} is biased to be (a)(d)2.0V, (b)(e)0.0V and (c)(f)-2.0V. The left(right) column provide the BP(MoS$_2$) conduction and valence band profile. Energy resolved carrier density for k$_x$=0(k$_x$=0.35) is overlaid with contour plots. Spatially resolved recombination current is provided with red lines/axis.
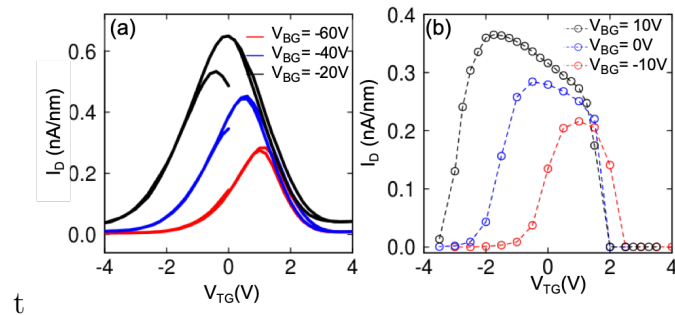
Fig. 6.5.: (a) IV curve measured from device in Fig.6.1(a). (b) Simulated AAP curve with device shown in Fig.6.1(b). The rate coefficient is set to be $6 \times 10^{-11} cm^{-3} s^{-1}$ with L = 10 nm .
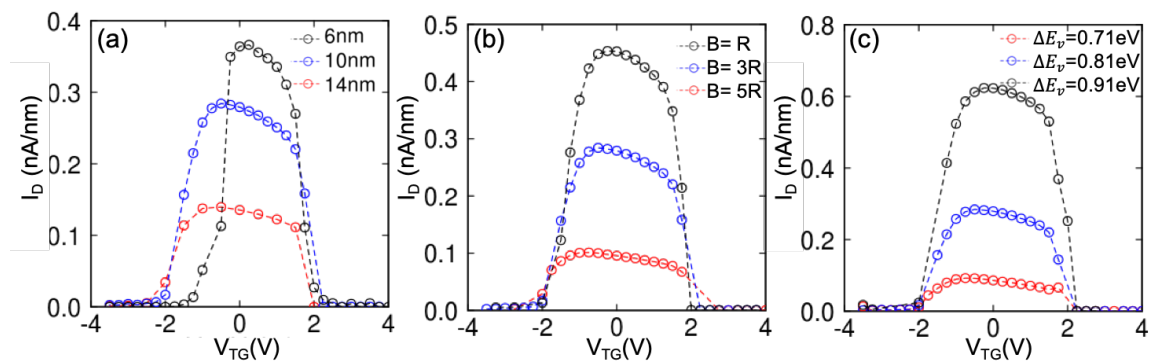
Fig. 6.6.: (a) $V_{BG} = 0$ and B=$6 \times 10^{-11} cm^3 s^{-1}$ are set with altering overlapping length,L. (b) V_{TG} is sweeped with V_{BG}=0 and L =10nm altering the Langevin recombination rates as labeled. The R is $2 \times 10^{-11} cm^3 s^{-1}$. (c) Band alignment between the BP and MoS$_2$ is altered.

REFERENCES

REFERENCES

[1] N. Consulting, "Energy Savings Forecast of Solid-State Lighting in General Illumination Applications," *U.S. Department of Energy Report*, no. August, pp. 2013–2014, 2016.

[2] S. Pimputkar, J. S. Speck, S. P. Denbaars, and S. Nakamura, "Prospects for LED lighting," *Nature Photonics*, vol. 3, no. 4, pp. 180–182, 2009.

[3] R. A. Oliver, S. E. Bennett, T. Zhu, D. J. Beesley, M. J. Kappers, D. W. Saxey, A. Cerezo, and C. J. Humphreys, "Microstructural origins of localization in InGaN quantum wells," *Journal of Physics D: Applied Physics*, vol. 43, no. 35, 2010.

[4] Y.-R. Wu, R. Shivaraman, K.-C. Wang, and J. S. Speck, "Analyzing the physical properties of InGaN multiple quantum well light emitting diodes from nano scale structure," *Applied Physics Letters*, vol. 101, no. 8, p. 083505, 2012. [Online]. Available: http://aip.scitation.org/doi/10.1063/1.4747532

[5] M. Piccardo, C. K. Li, Y. R. Wu, J. S. Speck, B. Bonef, R. M. Farrell, M. Filoche, L. Martinelli, J. Peretti, and C. Weisbuch, "Localization landscape theory of disorder in semiconductors. II. Urbach tails of disordered quantum well layers," *Physical Review B*, vol. 95, no. 14, pp. 1–12, 2017.

[6] M. A. Reshchikov and H. Morko, "Luminescence properties of defects in GaN," *Journal of Applied Physics*, vol. 97, no. 6, 2005.

[7] A. K. Reza, M. K. Hassan, and K. Roy, "Büttiker Probe-Based Modeling of TDDB: Application to Dielectric Breakdown in MTJs and MOS Devices," *IEEE Transactions on Electron Devices*, vol. 64, no. 8, pp. 3337–3345, 2017.

[8] A. K. Geim and I. V. Grigorieva, "Van der Waals heterostructures," *Nature*, vol. 499, no. 7459, pp. 419–425, 2013. [Online]. Available: http://www.ncbi.nlm.nih.gov/pubmed/23887427http://dx.doi.org/10.1038/nature12385%5Cnpapers3://publication/doi/10.1038/nature12385http://dx.doi.org/10.1038/nature12385

[9] C.-h. Lee, G.-h. Lee, A. M. van der Zande, W. Chen, Y. Li, M. Han, X. Cui, G. Arefe, C. Nuckolls, T. F. Heinz, J. Guo, J. Hone, P. Kim, A. M. V. D. Zande, W. Chen, Y. Li, M. Han, X. Cui, G. Arefe, C. Nuckolls, T. F. Heinz, J. Guo, J. Hone, P. Kim, A. M. van der Zande, W. Chen, Y. Li, M. Han, X. Cui, G. Arefe, C. Nuckolls, T. F. Heinz, J. Guo, J. Hone, P. Kim, A. M. V. D. Zande, W. Chen, Y. Li, M. Han, X. Cui, G. Arefe, C. Nuckolls, T. F. Heinz, J. Guo, J. Hone, P. Kim, A. M. van der Zande, W. Chen, Y. Li, M. Han, X. Cui, G. Arefe, C. Nuckolls, T. F. Heinz, J. Guo, J. Hone, P. Kim, A. M. V. D. Zande, W. Chen, Y. Li, M. Han, X. Cui, G. Arefe, C. Nuckolls, T. F. Heinz, J. Guo, J. Hone, and

P. Kim, "Atomically thin p-n junctions with van der Waals heterointerfaces." *Nature nanotechnology*, vol. 9, no. 9, pp. 1–29, 2014. [Online]. Available: http://www.nature.com/doifinder/10.1038/nnano.2014.150http://dx.doi.org/10.1038/nnano.2014.150http://www.ncbi.nlm.nih.gov/pubmed/25108809

[10] H. Yu, A. Kutana, and B. I. Yakobson, "Carrier Delocalization in Two-Dimensional Coplanar p-n Junctions of Graphene and Metal Dichalcogenides," *Nano Letters*, vol. 16, no. 8, pp. 5032–5036, 2016.

[11] Y. Li, Y. Wang, L. Huang, X. Wang, X. Li, H. X. Deng, Z. Wei, and J. Li, "Anti-Ambipolar Field-Effect Transistors Based on Few-Layer 2D Transition Metal Dichalcogenides," *ACS Applied Materials and Interfaces*, vol. 8, no. 24, pp. 15 574–15 581, 2016.

[12] T. Roy, M. Tosun, X. Cao, H. Fang, D.-H. Lien, P. Zhao, Y.-Z. Chen, Y.-L. Chueh, J. Guo, and A. Javey, "Dual-Gated MoS 2 /WSe 2 van der Waals Tunnel Diodes and Transistors," *ACS Nano*, vol. 9, no. 2, pp. 2071–2079, 2015. [Online]. Available: http://dx.doi.org/10.1021/nn507278b%5Cnhttp://pubs.acs.org.gaelnomade.ujf-grenoble.fr/doi/pdf/10.1021/nn507278b

[13] "Crosslight Website." [Online]. Available: http://crosslight.com/products/apsys/

[14] "silvaco website." [Online]. Available: https://www.silvaco.com/products/vwf/atlas/2D/led/ledbr.html/

[15] "str website."

[16] J. Geng, P. Sarangapani, K. C. Wang, E. Nelson, B. Browne, C. Wordelman, J. Charles, Y. Chu, T. Kubis, and G. Klimeck, "Quantitative Multi-Scale, Multi-Physics Quantum Transport Modeling of GaN-Based Light Emitting Diodes," *Physica Status Solidi (A) Applications and Materials Science*, vol. 215, no. 9, pp. 1–7, 2018.

[17] J. C. Slater and G. F. Koster, "Simplified LCAO method for the periodic potential problem," *Physical Review*, vol. 94, no. 6, pp. 1498–1524, 1954.

[18] N. Marzari, A. A. Mostofi, J. R. Yates, I. Souza, and D. Vanderbilt, "Maximally localized Wannier functions: Theory and applications," *Reviews of Modern Physics*, vol. 84, no. 4, pp. 1419–1475, 2012.

[19] S. Datta, *Quantum Transport : Atom to Transistor*, ser. . Cambridge: Cambridge University Press, 2005. [Online]. Available: http://ebooks.cambridge.org/ref/id/CBO9781139164313http://books.google.com/books?hl=en&lr=&id=Yj50EJoS224C&oi=fnd&pg=PR9&dq=Quantum+Transport+:+Atom+to+Transistor&ots=jmVfovCmEu&sig=oYLWTfZuNxd44-WwK4FwD-Tmg98

[20] Y. Tan, M. Povolotskyi, T. Kubis, T. B. Boykin, and G. Klimeck, "Transferable tight-binding model for strained group IV and III-V materials and heterostructures," *Physical Review B*, 2016.

[21] J. C. Slater and G. F. Koster, "Simplified LCAO method for the periodic potential problem," *Physical Review*, vol. 94, no. 6, pp. 1498–1524, 1954.

[22] N. J. Giordano, H. Nakanishi, and E. Ayars, *Computational Physics (second edition)*, 2006, vol. 74, no. 7. [Online]. Available: http://link.aip.org/link/AJPIAS/v74/i7/p652/s1&Agg=doi

[23] K. S. Novoselov, D. Jiang, F. Schedin, T. J. Booth, V. V. Khotkevich, S. V. Morozov, and A. K. Geim, "Two-dimensional atomic crystals," *Proceedings of the National Academy of Sciences of the United States of America*, vol. 102, no. 30, pp. 10 451–10 453, 2005. [Online]. Available: http://www.pnas.org/content/102/30/10451.abstract://www.ncbi.nlm.nih.gov/pmc/articles/PMC1180777/pdf/pnas-0502848102.pdf

[24] B. Radisavljevic, A. Radenovic, J. Brivio, V. Giacometti, and A. Kis, "Single-layer MoS2 transistors," *Nature nanotechnology*, vol. 6, no. 3, pp. 147–150, 2011.

[25] W. S. Yun, S. Han, S. C. Hong, I. G. Kim, and J. Lee, "Thickness and strain effects on electronic structures of transition metal dichalcogenides: 2H-MX_{2} semiconductors (M = Mo, W; X = S, Se, Te)," *Physical Review B*, vol. 85, no. 3, pp. 1–5, 2012.

[26] C. Zhu, D. Du, and Y. Lin, "Graphene-like 2D nanomaterial-based biointerfaces for biosensing applications," *Biosensors and Bioelectronics*, vol. 89, pp. 43–55, 2017. [Online]. Available: http://dx.doi.org/10.1016/j.bios.2016.06.045

[27] D. Jariwala, V. K. Sangwan, L. J. Lauhon, T. J. Marks, and M. C. Hersam, "Emerging device applications for semiconducting two-dimensional transition metal dichalcogenides," *ACS Nano*, vol. 8, no. 2, pp. 1102–1120, 2014.

[28] K. Kalantar-zadeh and J. Z. Ou, "Biosensors Based on Two-Dimensional MoS ¡sub¿2¡/sub¿," *ACS Sensors*, vol. 1, no. 1, pp. 5–16, 2016. [Online]. Available: http://pubs.acs.org/doi/abs/10.1021/acssensors.5b00142

[29] M. R. Esmaeili-Rad and S. Salahuddin, "High Performance Molybdenum Disulfide Amorphous Silicon Heterojunction Photodetector," *Scientific Reports*, vol. 3, p. 2345, 2013. [Online]. Available: http://www.pubmedcentral.nih.gov/articlerender.fcgi?artid=3731647&tool=pmcentrez&rendertype=abstract://www.nature.com/articles/srep02345

[30] J. S. Ross, P. Klement, A. M. Jones, N. J. Ghimire, J. Yan, M. G., T. Taniguchi, K. Watanabe, K. Kitamura, W. Yao, D. H. Cobden, and X. Xu, "Electrically tunable excitonic light-emitting diodes based on monolayer WSe2 p-n junctions," *Nat Nano*, vol. 9, no. 4, pp. 268–272, 2014. [Online]. Available: http://dx.doi.org/10.1038/nnano.2014.26%5Cnhttp://10.1038/nnano.2014.26%5Cnhttp://www.nature.com/nnano/journal/v9/n4/abs/nnano.2014.26.html#supplementary-information

[31] M. S. Choi, D. Qu, D. Lee, X. Liu, K. Watanabe, T. Taniguchi, and W. J. Yoo, "Lateral MoS2 p-n junction formed by chemical doping for use in high-performance optoelectronics," *ACS Nano*, vol. 8, no. 9, pp. 9332–9340, 2014.

[32] F. Withers, O. Del Pozo-Zamudio, A. Mishchenko, a. P. Rooney, A. Gholinia, K. Watanabe, T. Taniguchi, S. J. Haigh, a. K. Geim, a. I. Tartakovskii, and K. S. Novoselov, "Light-emitting diodes by band-structure engineering in van der Waals heterostructures," *Nature*

Materials, vol. 14, no. February, pp. 301–306, 2015. [Online]. Available: http://www.nature.com/doifinder/10.1038/nmat4205

[33] S. Bertolazzi, D. Krasnozhon, and A. Kis, "Nonvolatile memory cells based on MoS2/graphene heterostructures," *ACS Nano*, vol. 7, no. 4, pp. 3246–3252, 2013.

[34] V. K. Sangwan, D. Jariwala, I. S. Kim, K.-S. Chen, T. J. Marks, L. J. Lauhon, and M. C. Hersam, "Gate-tunable memristive phenomena mediated by grain boundaries in single-layer MoS2," *Nature Nanotechnology*, vol. 10, no. 5, pp. 403–406, 2015. [Online]. Available: http://www.nature.com/doifinder/10.1038/nnano.2015.56

[35] Z. Q. Zheng, T. M. Zhang, J. D. Yao, Y. Zhang, J. R. Xu, and G. W. Yang, "Flexible, transparent and ultra-broadband photodetector based on large-area WSe2 film for wearable devices," *Nanotechnology*, vol. 27, no. 22, p. 11, 2016. [Online]. Available: http://dx.doi.org/10.1088/0957-4484/27/22/225501

[36] J. Y. Oh, J. H. Lee, S. W. Han, S. S. Chae, E. J. Bae, Y. H. Kang, W. J. Choi, S. Y. Cho, J.-O. Lee, H. K. Baik, and T. I. Lee, "Chemically exfoliated transition metal dichalcogenide nanosheet-based wearable thermoelectric generators," *Energy Environ. Sci.*, vol. 9, no. 5, pp. 1696–1705, 2016. [Online]. Available: http://pubs.rsc.org/en/content/articlehtml/2016/ee/c5ee03813h%5Cnhttp://pubs.rsc.org/en/Content/ArticleLanding/2016/EE/C5EE03813H%5Cnhttp://xlink.rsc.org/?DOI=C5EE03813H

[37] F. Bonaccorso, A. Lombardo, T. Hasan, Z. Sun, L. Colombo, and A. C. Ferrari, "Production, Processing and Placement of Graphene and Two Dimensional Crystals," *Materials Today*, no. 15, pp. 564–589, 2012. [Online]. Available: http://arxiv.org/abs/1212.3319

[38] L. Britnell, R. M. Ribeiro, A. Eckmann, R. Jalil, B. D. Belle, A. Mishchenko, Y. Kim, R. V. Gorbachev, T. Georgiou, S. V. Morozov, A. N. Grigorenko, A. K. Geim, C. Casiraghi, A. H. C. Neto, and K. S. Novoselov, "Strong Light-Matter Interactions in heterostructures of atomically Thin Films," *Science*, vol. 340, no. 6238, pp. 1331–1314, 2013.

[39] S. L. Howell, D. Jariwala, C. C. Wu, K. S. Chen, V. K. Sangwan, J. Kang, T. J. Marks, M. C. Hersam, and L. J. Lauhon, "Investigation of Band-Offsets at Monolayer-Multilayer MoS¡inf¿2¡/inf¿ Junctions by Scanning Photocurrent Microscopy," *Nano Letters*, vol. 15, no. 4, pp. 2278–2284, 2015.

[40] F. W. Chen, H. Ilatikhameneh, T. A. Ameen, G. Klimeck, and R. Rahman, "Thickness Engineered Tunnel Field-Effect Transistors based on Phosphorene," *arXiv preprint arXiv:1607.04065*, 2016.

[41] X. Zhu, N. R. Monahan, Z. Gong, H. Zhu, K. W. Williams, and C. A. Nelson, "Charge Transfer Excitons at van der Waals Interfaces," *Journal of the American Chemical Society*, vol. 137, no. 26, pp. 8313–8320, 2015.

[42] H. Chen, X. Wen, J. Zhang, T. Wu, Y. Gong, X. Zhang, J. Yuan, C. Yi, J. Lou, P. M. Ajayan, W. Zhuang, G. Zhang, and J. Zheng, "Ultrafast formation of interlayer hot excitons in atomically thin MoS2/WS2 heterostructures," *Nature Communications*, vol. 7, p. 12512, 2016. [Online]. Available: http://www.nature.com/doifinder/10.1038/ncomms12512

[43] T. Chu, H. Ilatikhameneh, G. Klimeck, R. Rahman, and Z. Chen, "Electrically Tunable Bandgaps in Bilayer MoS2," *Nano Letters*, vol. 15, no. 12, pp. 8000–8007, 2015.

[44] J. Klein, J. Wierzbowski, A. Regler, J. Becker, F. Heimbach, K. Müller, M. Kaniber, and J. J. Finley, "Stark Effect Spectroscopy of Mono- and Few-Layer MoS2," *Nano Letters*, vol. 16, no. 3, pp. 1554–1559, 2016.

[45] . Szabó, R. Rhyner, and M. Luisier, "Ab initio simulation of single- and few-layer MoS2 transistors: Effect of electron-phonon scattering," *Physical Review B - Condensed Matter and Materials Physics*, vol. 92, no. 3, pp. 1–10, 2015. [Online]. Available: http://link.aps.org/doi/10.1103/PhysRevB.92.035435

[46] H. Ilatikhameneh, Y. Tan, B. Novakovic, G. Klimeck, R. Rahman, and J. Appenzeller, "Tunnel Field-Effect Transistors in 2D Transition Metal Dichalcogenide Materials," *IEEE Journal on Exploratory Solid-State Computational Devices and Circuits*, vol. 1, no. 2, pp. 1–7, 2015.

[47] S. Fang, R. Kuate Defo, S. N. Shirodkar, S. Lieu, G. A. Tritsaris, and E. Kaxiras, "Ab initio tight-binding Hamiltonian for transition metal dichalcogenides," *Physical Review B - Condensed Matter and Materials Physics*, vol. 92, no. 20, p. 205108, 2015.

[48] J. Maassen, M. Harb, V. Michaud-Rioux, Y. Zhu, and H. Guo, "Quantum transport modeling from first principles," *Proc. IEEE*, vol. 101, no. 2, pp. 518–530, 2013.

[49] "http://cms.mpi.univie.ac.at/vasp/vasp.pdf," 2015. [Online]. Available: http://cms.mpi.univie.ac.at/vasp/vasp.pdf

[50] "http://www.arscryo.com/CS204_F-DMX-20-OM.html," 2016. [Online]. Available: http://www.arscryo.com/CS204_F-DMX-20-OM.html

[51] "http://www.andor.com/spectrograph/shamrock-spectrograph-series/shamrock-303i," 2016. [Online]. Available: http://www.andor.com/spectrograph/shamrock-spectrograph-series/shamrock-303i

[52] S. Steiger, M. Povolotskyi, H. H. Park, T. Kubis, and G. Klimeck, "NEMO5: A parallel multiscale nanoelectronics modeling tool," *IEEE Transactions on Nanotechnology*, vol. 10, no. 6, pp. 1464–1474, 2011.

[53] G. Kresse and J. Furthmüller, "Efficient iterative schemes for ab initio total-energy calculations using a plane-wave basis set," *Physical Review B*, vol. 54, no. 16, pp. 11 169–11 186, 1996.

[54] T. Bučko, J. Hafner, S. Lebègue, and J. G. Ángyán, "Improved Description of the Structure of Molecular and Layered Crystals: Ab Initio DFT Calculations with van der Waals Corrections," *The Journal of Physical Chemistry A*, vol. 114, no. 43, pp. 11 814–11 824, 2010. [Online]. Available: http://dx.doi.org/10.1021/jp106469x

[55] F. Jellinek, G. Brauer, and H. Müller, "Molybdenum and Niobium Sulphides," *Nature*, vol. 185, no. 4710, pp. 376–377, 2 1960. [Online]. Available: http://dx.doi.org/10.1038/185376a0

[56] W. Wei, Y. Dai, C. Niu, and B. Huang, "Controlling the Electronic Structures and Properties of in-Plane Transition-Metal Dichalcogenides Quantum Wells," *Scientific Reports*, vol. 5, pp. 17 578 EP –, 11 2015. [Online]. Available: http://dx.doi.org/10.1038/srep17578

[57] J. P. Perdew, K. Burke, and Y. Wang, "Generalized gradient approximation for the exchange-correlation hole of a many-electron system," *Physical Review B*, vol. 54, no. 23, pp. 16 533–16 539, 1996.

[58] N. Marzari and D. Vanderbilt, "Maximally-localized generalized Wannier functions for composite energy bands," *Physical Review B*, vol. 56, no. 20, p. 12847, 1997. [Online]. Available: http://arxiv.org/abs/cond-mat/9707145

[59] R. Das, S. K. Pandey, and P. Mahadevan, "Layer dependent electronic structure changes in transition metal dichalcogenides-The role of geometric confinement," pp. 1–17, 2017.

[60] D. Jariwala, V. K. Sangwan, D. J. Late, J. E. Johns, V. P. Dravid, T. J. Marks, L. J. Lauhon, and M. C. Hersam, "Band-like transport in high mobility unencapsulated single-layer MoS2 transistors," *Applied Physics Letters*, vol. 102, no. 2013, p. 173107, 2013. [Online]. Available: http://ieeexplore.ieee.org/xpls/abs_all.jsp?arnumber=6512467%5Cnhttp://link.aip.org/link/APPLAB/v102/i17/p173107/s1&Agg=doi

[61] S. Saito, K. Torii, M. Hiratani, and T. Onai, "Analytical quantum mechanical model for accumulation capacitance of MOS structures," *IEEE Electron Device Letters*, vol. 23, no. 6, pp. 348–350, 6 2002.

[62] A. Novikov, "Experimental measurement of work function in doped silicon surfaces," *Solid-State Electronics*, vol. 54, no. 1, pp. 8–13, 2010.

[63] X. Chen, Z. Wu, S. Xu, L. Wang, R. Huang, Y. Han, W. Ye, W. Xiong, T. Han, G. Long, Y. Wang, Y. He, Y. Cai, P. Sheng, and N. Wang, "Probing the electron states and metal-insulator transition mechanisms in molybdenum disulphide vertical heterostructures," *Nature Communications*, vol. 6, p. 6088, 2015. [Online]. Available: http://www.nature.com/ncomms/2015/150114/ncomms7088/full/ncomms7088.html

[64] P. Sarangapani, D. Mejia, J. Charles, W. Gilbertson, H. Ilatikhameneh, T. Ameen, A. Roche, J. Fonseca, and G. Klimeck, "Quantum dot lab: an online platform for quantum dot simulations," in *2015 International Workshop on Computational Electronics (IWCE)*, 9 2015, pp. 1–3.

[65] K. Liu, L. Zhang, T. Cao, C. Jin, D. Qiu, Q. Zhou, A. Zettl, P. Yang, S. G. Louie, and F. Wang, "Evolution of interlayer coupling in twisted molybdenum disulfide bilayers," *Nature Communications*, vol. 5, pp. 1–6, 1. [Online]. Available: http://www.ncbi.nlm.nih.gov/pubmed/25233054%5Cnhttp://dx.doi.org/10.1038/ncomms5966

[66] L. Zhang and A. Zunger, "Evolution of electronic structure as a function of layer thickness in group-VIB transition metal dichalcogenides: Emergence of localization prototypes," *Nano Letters*, vol. 15, no. 2, pp. 949–957, 2015.

[67] J. Kang, L. Zhang, and S. H. Wei, "A Unified Understanding of the Thickness-Dependent Bandgap Transition in Hexagonal Two-Dimensional Semiconductors," *Journal of Physical Chemistry Letters*, vol. 7, no. 4, pp. 597–602, 2016.

[68] H.-M. Li, D. Lee, D. Qu, X. Liu, J. Ryu, A. Seabaugh, and W. J. Yoo, "Ultimate thin vertical p-n junction composed of two-dimensional layered molybdenum disulfide." *Nature communications*, vol. 6, p. 6564, 2015. [Online]. Available: http://www.nature.com/ncomms/2015/150324/ncomms7564/full/ncomms7564.html

[69] Y. Jin, D. H. Keum, S. J. An, J. Kim, H. S. Lee, and Y. H. Lee, "A Van der Waals Homojunction: Ideal p-n Diode Behavior in MoSe$_2$," *Advanced Materials*, vol. 27, no. 37, pp. 5534–5540, 2015.

[70] D. Ovchinnikov, A. Allain, Y. S. Huang, D. Dumcenco, and A. Kis, "Electrical transport properties of single-layer WS2," *ACS Nano*, vol. 8, no. 8, pp. 8174–8181, 2014.

[71] J. A. Wilson and A. D. Yoffe, "The transition metal dichalcogenides discussion and interpretation of the observed optical, electrical and structural properties," *Advances in Physics*, vol. 18, pp. 193–335, 5 1969.

[72] R. Akashi, M. Ochi, S. Bordács, R. Suzuki, Y. Tokura, Y. Iwasa, and R. Arita, "Two-dimensional valley electrons and excitons in noncentrosymmetric 3R-MoS2," *Physical Review Applied*, vol. 4, no. 1, pp. 1–7, 2015.

[73] Y. Li, Y. Rao, K. F. Mak, Y. You, S. Wang, C. R. Dean, and T. F. Heinz, "Probing Symmetry Properties of Few-Layer MoS$_2$ and h-BN by Optical Second-Harmonic Generation," *Nano Letters*, pp. 3329–3333, 2013. [Online]. Available: http://www.ncbi.nlm.nih.gov/pubmed/23718906

[74] K. Komider, J. W. González, and J. Fernández-Rossier, "Large spin splitting in the conduction band of transition metal dichalcogenide monolayers," *Physical Review B - Condensed Matter and Materials Physics*, vol. 88, no. 24, pp. 1–7, 2013.

[75] J. R. Schaibley, H. Yu, G. Clark, P. Rivera, J. S. Ross, K. L. Seyler, W. Yao, and X. Xu, "Valleytronics in 2D materials," *Nature Reviews Materials*, vol. 1, no. 11, p. 16055, 2016. [Online]. Available: http://www.nature.com/articles/natrevmats201655

[76] A. M. Jones, H. Yu, J. S. Ross, P. Klement, N. J. Ghimire, J. Yan, D. G. Mandrus, W. Yao, and X. Xu, "Spinlayer locking effects in optical orientation of exciton spin in bilayer WSe2," *Nature Physics*, vol. 10, no. 2, pp. 130–134, 2014. [Online]. Available: http://dx.doi.org/10.1038/nphys2848http://www.nature.com/doifinder/10.1038/nphys2848

[77] Z. Gong, G.-b. Liu, H. Yu, D. Xiao, X. Cui, X. Xu, and W. Yao, "Magnetoelectric effects and valley-controlled spin quantum gates in transition metal dichalcogenide bilayers." *Nature communications*, vol. 4, no. May, p. 2053, 2013. [Online]. Available: http://dx.doi.org/10.1038/ncomms3053http://www.ncbi.nlm.nih.gov/pubmed/23784147

[78] X. Xu, "Spin and pseudospins in transition metal dichalcogenides," *Proceedings - 2014 Summer Topicals Meeting Series, SUM 2014*, vol. 10, no. April, pp. 1–2, 2014.

[79] K. F. Mak, C. Lee, J. Hone, J. Shan, and T. F. Heinz, "Atomically thin MoS2: A new direct-gap semiconductor," *Physical Review Letters*, vol. 105, no. 13, pp. 2–5, 2010.

[80] J. G. Kim, W. S. Yun, S. Jo, J. Lee, and C.-h. Cho, "Effect of interlayer interactions on exciton luminescence in atomic- layered MoS 2 crystals," *Scientific Reports*, no. April, pp. 1–7, 2016. [Online]. Available: http://dx.doi.org/10.1038/srep29813

[81] J. Piprek, "Efficiency droop in nitride-based light-emitting diodes," *Physica Status Solidi (A) Applications and Materials Science*, vol. 207, no. 10, pp. 2217–2225, 2010.

[82] R. N. Hall, "Electron-Hole Recombination in Germanium," *Phys. Rev.*, vol. 87, no. 2, p. 387, 7 1952. [Online]. Available: https://link.aps.org/doi/10.1103/PhysRev.87.387

[83] S. L. Chuang, *Physics of Optoelectronic Devices*, ser. Wiley Series in Pure and Applied Optics. Wiley, 1995. [Online]. Available: https://books.google.com/books?id=ect6QgAACAAJ

[84] D. Vasileska, "Drift-Diffusion Model: Introduction." [Online]. Available: https://nanohub.org/resources/1545/download/ddmodel_introductory_part_word.pdf

[85] "nanobte." [Online]. Available: https://nanohub.org/resources/12229

[86] M. Luisier, "Atomistic modeling of anharmonic phonon-phonon scattering in nanowires," *Physical Review B - Condensed Matter and Materials Physics*, vol. 86, no. 24, pp. 1–10, 2012.

[87] S. Datta, "Nanoscale device modeling: the Green's function method," *Superlattices and Microstructures*, vol. 28, no. 4, pp. 253–278, 2000.

[88] R. Venugopal, M. Paulsson, S. Goasguen, S. Datta, and M. S. Lundstrom, "A simple quantum mechanical treatment of scattering in nanoscale transistors," *Journal of Applied Physics*, vol. 93, no. 9, pp. 5613–5625, 2003.

[89] K. Miao, S. Sadasivam, J. Charles, G. Klimeck, T. S. Fisher, and T. Kubis, "Bü ttiker probes for dissipative phonon quantum transport in semiconductor nanostructures," vol. 113107, pp. 1–9, 2016.

[90] M. Bttiker and M. Buettiker, "Role of quantum coherence in series resistors," *Physical Review B*, vol. 33, no. 5, pp. 3020–3026, 1986.

[91] S. Datta, *Electronic Transport in mesoscopic systems*, 1997. [Online]. Available: http://books.google.com/books?hl=en&lr=&id=28BC-ofEhvUC&oi=fnd&pg=PR12&dq=Electronic+transport+in+mesoscopic+System&ots=mJSYGt4pok&sig=y3g4gKAu0gy_AlPmouHrZHnln68

[92] ——, *Lessons from Nanoelectronics: A New Perspective on Transport*, ser. Lessons from nanoscience. World Scientific Publishing Company, 2012. [Online]. Available: https://books.google.com/books?id=JO-pcQAACAAJ

[93] M. P. Anantram, M. S. Lundstrom, and D. E. Nikonov, "Modeling of nanoscale devices," *Proceedings of the IEEE*, vol. 96, no. 9, pp. 1511–1550, 2008.

[94] R. Lake, G. Klimeck, R. C. Bowen, and D. Jovanovic, "Single and multiband modeling of quantum electron transport through layered semiconductor devices," *Journal of Applied Physics*, vol. 81, no. 12, p. 7845, 1997. [Online]. Available: http://scitation.aip.org/content/aip/journal/jap/81/12/10.1063/1.365394

[95] a. Svizhenko, M. P. Anantram, T. R. Govindan, B. Biegel, and R. Venugopal, "Two-dimensional quantum mechanical modeling of nanotransistors," *Journal of Applied Physics*, vol. 91, no. 2002, pp. 2343–2354, 2002.

[96] S. Sadasivam, N. Ye, J. P. Feser, J. Charles, K. Miao, T. Kubis, and T. S. Fisher, "Thermal transport across metal silicide-silicon interfaces: First-principles calculations and Green's function transport simulations," *Physical Review B*, vol. 95, no. 8, pp. 1–15, 2017.

[97] M. P. L. Sancho, J. M. L. Sancho, and J. Rubio, "Quick iterative scheme for the calculation of transfer matrices: application to Mo (100)," *Journal of Physics F: Metal Physics*, vol. 14, no. 5, pp. 1205–1215, 5 1984. [Online]. Available: http://stacks.iop.org/0305-4608/14/i=5/a=016?key=crossref.73654bb2c5e7ede93601a4f4e5f6247b

[98] M. P. L. Sancho, J. M. L. Sancho, J. M. L. Sancho, J. Rubio, H. Search, C. Journals, A. Contact, M. Iopscience, and I. P. Address, "Highly convergent schemes for the calculation of bulk and surface Green functions," *Journal of Physics F: Metal Physics*, vol. 15, no. 4, pp. 851–858, 1985. [Online]. Available: http://iopscience.iop.org/0305-4608/15/4/009

[99] C.-s. Pang, C.-y. Chen, T. Ameen, S. Zhang, H. Ilatikhameneh, R. Rahman, G. Klimeck, and Z. Chen, "WSe 2 Homojunction Devices : Electrostatically Configurable as Diodes , MOSFETs , and Tunnel FETs for Reconfigurable Computing," vol. 1902770, pp. 1–8, 2019.

[100] P. Krogstrup, H. I. Jørgensen, M. Heiss, O. Demichel, J. V. Holm, M. Aagesen, J. Nygard, and A. Fontcuberta I Morral, "Single-nanowire solar cells beyond the Shockley-Queisser limit," *Nature Photonics*, vol. 7, no. 4, pp. 306–310, 2013.

[101] H. Ilatikhameneh, T. A. Ameen, C. Chen, G. Klimeck, and R. Rahman, "Sensitivity Challenge of Steep Transistors," *IEEE Transactions on Electron Devices*, 2018.

[102] J. Charles, P. Sarangapani, R. Golizadeh-Mojarad, R. Andrawis, D. Lemus, X. Guo, D. Mejia, J. E. Fonseca, M. Povolotskyi, T. Kubis, and G. Klimeck, "Incoherent transport in NEMO5: realistic and efficient scattering on phonons," *Journal of Computational Electronics*, vol. 15, no. 4, pp. 1123–1129, 2016.

[103] M. Burgelman, P. Nollet, and S. Degrave, "Modelling polycrystalline semiconductor solar cells," *Thin Solid Films*, vol. 361, pp. 527–532, 2000.

[104] K.-c. Wang and Y.-r. Wu, "Transition Rate in the InGaN Quantum Dot Intermediate-Band Solar Cell," pp. 822–825, 2011.

[105] C. Jirauschek and T. Kubis, "Modeling techniques for quantum cascade lasers," *Applied Physics Reviews*, vol. 1, no. 1, 2014.

[106] P. Ghedini, D. Agopian, M. Dalla, V. Martino, S. Gomes, J. Antonio, R. Rooyackers, D. Leonelli, and C. Claeys, "Solid-State Electronics Temperature impact on the tunnel fet off-state current components," *Solid State Electronics*, vol. 78, pp. 141–146, 2012. [Online]. Available: http://dx.doi.org/10.1016/j.sse.2012.05.053

[107] Q. Smets, A. S. Verhulst, E. Simoen, D. Gundlach, C. Richter, N. Collaert, and M. M. Heyns, "Calibration of Bulk Trap-Assisted Tunneling and Shockley-Read-Hall Currents and Impact on InGaAs Tunnel-FETs," *IEEE Transactions on Electron Devices*, vol. 64, no. 9, pp. 3622–3626, 2017.

[108] G. Klimeck, R. Lake, R. C. Bowen, W. R. Frensley, and T. S. Moise, "Quantum device simulation with a generalized tunneling formula," *Applied Physics Letters*, vol. 67, no. June 1995, p. 2539, 1995.

[109] U. Aeberhard, "Quantum-kinetic perspective on photovoltaic device operation in nanostructure-based solar cells," *Journal of Materials Research*, vol. 33, no. 4, pp. 373–386, 2018.

[110] ——, "Nonequilibrium Green's function picture of nonradiative recombination of the Shockley-Read-Hall type," *Physical Review B*, vol. 99, no. 12, p. 125302, 2019. [Online]. Available: https://doi.org/10.1103/PhysRevB.99.125302

[111] P. Greck, S. Birner, B. Huber, and P. Vogl, "Efficient method for the calculation of dissipative quantum transport in quantum cascade lasers," *Optics Express*, vol. 23, no. 5, p. 6587, 2015. [Online]. Available: https://www.osapublishing.org/abstract.cfm?URI=oe-23-5-6587

[112] A. Shedbalkar and B. Witzigmann, "Non equilibrium Greens function quantum transport for green multi-quantum well nitride light emitting diodes," *Optical and Quantum Electronics*, vol. 50, no. 2, pp. 1–10, 2018. [Online]. Available: https://doi.org/10.1007/s11082-018-1335-1

[113] "Atlas User Manual." [Online]. Available: https://www.silvaco.com/products/tcad/device_simulation/atlas/atlas.html

[114] M. H. Kim, M. F. Schubert, Q. Dai, J. K. Kim, E. F. Schubert, J. Piprek, and Y. Park, "Origin of efficiency droop in GaN-based light-emitting diodes," *Applied Physics Letters*, vol. 91, no. 18, pp. 1–4, 2007.

[115] S. Bandyopadhyay, M. E. Klausmeier-Brown, C. M. Maziar, S. Datta, and M. S. Lundstrom, "Rigorous Technique To Couple Monte Carlo and Drift-Diffusion Models for Computationally Efficient Device Simulation." *IEEE Transactions on Electron Devices*, vol. ED-34, no. 2, pp. 393–399, 1987.

[116] F. Bufler, A. Schenk, and W. Fichtner, "Monte Carlo, Hydrodynamic and Drift-Diffusion Simulation of Scaled Double-Gate MOSFETs," *Journal of Computational Electronics*, vol. 2, no. 2-4, pp. 81–84, 2004.

[117] P. Procel, P. Löper, F. Crupi, C. Ballif, and A. Ingenito, "Numerical simulations of hole carrier selective contacts in p-type c-Si solar cells," *Solar Energy Materials and Solar Cells*, vol. 200, no. January, p. 109937, 2019. [Online]. Available: https://doi.org/10.1016/j.solmat.2019.109937

[118] J. R. Lang, N. G. Young, R. M. Farrell, Y. R. Wu, and J. S. Speck, "Carrier escape mechanism dependence on barrier thickness and temperature in InGaN quantum well solar cells," *Applied Physics Letters*, vol. 101, no. 18, 2012.

[119] J. Wu, W. Walukiewicz, K. M. Yu, W. Shan, J. W. Ager, E. E. Haller, H. Lu, W. J. Schaff, W. K. Metzger, and S. Kurtz, "Superior radiation resistance of In1-xGaxN alloys: Full-solar-spectrum photovoltaic material system," *Journal of Applied Physics*, 2003.

[120] S. K. Jain, N. Aggarwal, S. Krishna, R. Kumar, S. Husale, V. Gupta, and G. Gupta, "GaN-UV photodetector integrated with asymmetric metal semiconductor metal structure for enhanced responsivity," *Journal of Materials Science: Materials in Electronics*, 2018.

[121] J. Wang, E. Polizzi, and M. Lundstrom, "A three-dimensional quantum simulation of silicon nanowire transistors with the effective-mass approximation," *Journal of Applied Physics*, vol. 96, no. 4, pp. 2192–2203, 2004.

[122] J. Z. Huang, K. Wang, W. R. Frensley, and G. Klimeck, "Finite difference schemes for k·p models: A comparative study," *18th International Workshop on Computational Electronics, IWCE 2015*, pp. 5–6, 2015.

[123] K. C. Wang, T. K. Stanev, D. Valencia, J. Charles, A. Henning, V. K. Sangwan, A. Lahiri, D. Mejia, P. Sarangapani, M. Povolotskyi, A. Afzalian, J. Maassen, G. Klimeck, M. C. Hersam, L. J. Lauhon, N. P. Stern, and T. Kubis, "Control of interlayer physics in 2H transition metal dichalcogenides," *Journal of Applied Physics*, vol. 122, no. 22, 2017.

[124] D. Valencia, E. Wilson, Z. Jiang, G. A. Valencia-Zapata, K. C. Wang, G. Klimeck, and M. Povolotskyi, "Grain-Boundary Resistance in Copper Interconnects: From an Atomistic Model to a Neural Network," *Physical Review Applied*, vol. 9, no. 4, p. 44005, 2018. [Online]. Available: https://doi.org/10.1103/PhysRevApplied.9.044005

[125] F. Zahid, M. Paulsson, E. Polizzi, A. W. Ghosh, L. Siddiqui, and S. Datta, "A self-consistent transport model for molecular conduction based on extended Hückel theory with full three-dimensional electrostatics A self-consistent transport model for molecular conduction based on extended Hückel theory with full three-dimensional el," vol. 064707, no. May 2014, 2012.

[126] C. Y. Chen, T. A. Ameen, H. Ilatikhameneh, R. Rahman, G. Klimeck, and J. Appenzeller, "Channel Thickness Optimization for Ultrathin and 2-D Chemically Doped TFETs," *IEEE Transactions on Electron Devices*, vol. 65, no. 10, pp. 4614–4621, 2018.

[127] S. K. Pugh, D. J. Dugdale, S. Brand, and R. A. Abram, "Electronic structure calculations on nitride semiconductors," *Semiconductor Science and Technology*, vol. 14, no. 1, pp. 23–31, 1999.

[128] A. Dmitriev and A. Oruzheinikov, "The rate of radiative recombination in the nitride semiconductors and alloys," vol. 86, no. January 1999, 1999.

[129] F. Olivier, A. Daami, C. Licitra, and F. Templier, "Shockley-Read-Hall and Auger non-radiative recombination in GaN based LEDs: A size effect study," *Applied Physics Letters*, 2017.

[130] F. Schäffl, "Properties of advanced semiconductor materials : GaN, AlN, InN, BN, SiC, SiGe," *John Wiley Sons Inc New York*, 2001.

[131] T. Kubis and P. Vogl, "Assessment of approximations in nonequilibrium Green's function theory," *Physical Review B - Condensed Matter and Materials Physics*, 2011.

[132] Franz Urbach, "The Long-Wavelength Edge of Photographic Sensitivity and of the Electronic Absorption of Solids," *Physical Review*, vol. 92, no. 5, pp. 1324–1324, 1953.

[133] P. Sarangapani, Y. Chu, K. C. Wang, D. Valencia, J. Charles, and T. Kubis, "Nonequilibrium Green's function method: Transport and band tail predictions in transition metal dichalcogenides," *International Conference on Simulation of Semiconductor Processes and Devices, SISPAD*, vol. 2018-Septe, pp. 38–39, 2018.

[134] T. T. Mnatsakanov, M. E. Levinshtein, L. I. Pomortseva, S. N. Yurkov, G. S. Simin, and M. A. Khan, "Carrier mobility model for GaN," *Solid-State Electronics*, vol. 47, no. 1, pp. 111–115, 2003.

[135] P. Sarangapani, Y. Chu, J. Charles, and T. Kubis, "Non-equilibrium Green's function predictions of band tails and band gap narrowing in III-V semiconductors and nanodevices," 2019. [Online]. Available: http://arxiv.org/abs/1904.07458

[136] T. Kubis, C. Yeh, P. Vogl, A. Benz, G. Fasching, and C. Deutsch, "Theory of nonequilibrium quantum transport and energy dissipation in terahertz quantum cascade lasers," *Physical Review B - Condensed Matter and Materials Physics*, 2009.

[137] C. de Falco, E. Gatti, A. L. Lacaita, and R. Sacco, "Quantum-corrected drift-diffusion models for transport in semiconductor devices," *Journal of Computational Physics*, 2005.

[138] C.-Y. Chen and Y.-R. Wu, "Studying the short channel effect in the scaling of the AlGaN/GaN nanowire transistors," *Journal of Applied Physics*, vol. 113, no. 21, p. 214501, 2013. [Online]. Available: https://doi.org/10.1063/1.4808241

[139] A. Latreche, "Combined thermionic emission and tunneling mechanisms for the analysis of the leakage current for Ga2O3 Schottky barrier diodes," *SN Applied Sciences*, vol. 1, no. 2, pp. 1–9, 2019. [Online]. Available: https://doi.org/10.1007/s42452-019-0192-2

[140] D. M. Tobnaghi, R. Madatov, and P. Farhadi, "Investigation of light intensity and temperature dependency of solar cells electric parameters," *Electric Power Engineering & Contol Systems 2013*, 2013.

[141] R. Frisenda, A. J. Molina-Mendoza, T. Mueller, A. Castellanos-Gomez, and H. S. Van Der Zant, "Atomically thin p-n junctions based on two-dimensional materials," *Chemical Society Reviews*, vol. 47, no. 9, pp. 3339–3358, 2018.

[142] M. Y. Li, Y. Shi, C. C. Cheng, L. S. Lu, Y. C. Lin, H. L. Tang, M. L. Tsai, C. W. Chu, K. H. Wei, J. H. He, W. H. Chang, K. Suenaga, and L. J. Li, "Epitaxial growth of a monolayer WSe¡inf¿2¡/inf¿-MoS¡inf¿2¡/inf¿ lateral p-n junction with an atomically sharp interface," *Science*, 2015.

[143] R. Zhou, V. Ostwal, and J. Appenzeller, "Vertical versus Lateral Two-Dimensional Heterostructures: On the Topic of Atomically Abrupt p/n-Junctions," *Nano Letters*, vol. 17, no. 8, pp. 4787–4792, 2017.

[144] D. Jariwala, V. K. Sangwan, C.-C. Wu, P. L. Prabhumirashi, M. L. Geier, T. J. Marks, L. J. Lauhon, and M. C. Hersam, "Gate-tunable carbon nanotube-MoS2 heterojunction p-n diode," *Proceedings of the National Academy of Sciences*, vol. 110, no. 45, pp. 18 076–18 080, 2013. [Online]. Available: http://www.pnas.org/cgi/doi/10.1073/pnas.1317226110

[145] V. K. Sangwan, M. E. Beck, A. Henning, J. Luo, H. Bergeron, J. Kang, I. Balla, H. Inbar, L. J. Lauhon, and M. C. Hersam, "Self-Aligned van der Waals Heterojunction Diodes and Transistors," *Nano Letters*, vol. 18, no. 2, pp. 1421–1427, 2018.

[146] D. Jariwala, V. K. Sangwan, J. W. T. Seo, W. Xu, J. Smith, C. H. Kim, L. J. Lauhon, T. J. Marks, and M. C. Hersam, "Large-area, low-voltage, anti-ambipolar heterojunctions from solution-processed semiconductors," *Nano Letters*, vol. 15, no. 1, pp. 416–421, 2015.

[147] M. Huang, S. Li, Z. Zhang, X. Xiong, X. Li, and Y. Wu, "Multifunctional high-performance van der Waals heterostructures," *Nature Nanotechnology*, no. October, pp. 1–8, 2017. [Online]. Available: http://www.nature.com/doifinder/10.1038/nnano.2017.208

[148] Z. Wang, X. He, X. X. Zhang, and H. N. Alshareef, "Hybrid van der Waals pn Heterojunctions based on SnO and 2D MoS2," *Advanced Materials*, vol. 28, no. 41, pp. 9133–9141, 2016.

[149] J. K. Kim, K. Cho, T. Y. Kim, J. Pak, J. Jang, Y. Song, Y. Kim, B. Y. Choi, S. Chung, W. K. Hong, and T. Lee, "Trap-mediated electronic transport properties of gate-tunable pentacene/MoS 2 p-n heterojunction diodes," *Scientific Reports*, vol. 6, no. November, pp. 1–8, 2016. [Online]. Available: http://dx.doi.org/10.1038/srep36775

[150] D. Jariwala, S. L. Howell, K. S. Chen, J. Kang, V. K. Sangwan, S. A. Filippone, R. Turrisi, T. J. Marks, L. J. Lauhon, and M. C. Hersam, "Hybrid, Gate-Tunable, van der Waals p-n Heterojunctions from Pentacene and MoS2," *Nano Letters*, vol. 16, no. 1, pp. 497–503, 2016.

[151] Z. Nie, Y. Wang, Z. Li, Y. Sun, S. Qin, X. Liu, I. C. E. Turcu, Y. Shi, R. Zhang, Y. Ye, Y. Xu, G. Cerullo, and F. Wang, " Ultrafast free carrier dynamics in black phosphorusmolybdenum disulfide (BP/MoS 2) heterostructures ," *Nanoscale Horizons*, pp. 18–23, 2019.

[152] K. C. Wang, Y. Chu, D. Valencia, J. Geng, J. Charles, P. Sarangapani, and T. Kubis, "Nonequilibrium Green's function method: Büttiker probes for carrier generation and recombination," *International Conference on Simulation of Semiconductor Processes and Devices, SISPAD*, vol. 2018-Septe, no. 1, pp. 5–8, 2018.

[153] K. C. Wang, Y. Chu, and T. Kubis, "Self-energies: Enabling multiphysics and multiscaling in optoelectronic quantum transport modeling," *Proceedings of the International Conference on Numerical Simulation of Optoelectronic Devices, NUSOD*, vol. 2018-Novem, pp. 49–50, 2018.

[154] L. Huang, N. Huo, Y. Li, H. Chen, J. Yang, Z. Wei, J. Li, and S. S. Li, "Electric-Field Tunable Band Offsets in Black Phosphorus and MoS2 van der Waals p-n Heterostructure," *Journal of Physical Chemistry Letters*, vol. 6, no. 13, pp. 2483–2488, 2015.

APPENDICES

A. WANNIER90 AND NEMO5 INTERFACE

A.1 Installation

- compile wannier90-2.1.0

    1. download from the official website

    2. make lib

    3. locate the path of libwannier.a which will be used next

- compile vasp.5.4.4.tar.gz with wannier90 libarary

    1. `cp arch/makefile.include.linux_intel  ./makefile.include`

    2. add the following changes:

        ```
        My prompt>diff arch/makefile.include.linux_intel  ./makefile.include
        10a11
        >   -DVASP2WANNIER90v2
        34a36
        > LLIBS += /home/wang2366/work/wannier90-2.1.0/libwannier.a
        ```

    3. make all

A.2 Wannierization

1. SCF calculation:

    (a) execute vasp

2. nscf bandstructure calculation. The output bandstructure can provide a benchmark of whether the wannier90 generated basis can reproduce the same bandstructure.

    (a) copy CHG CHGCAR WAVECAR from step 1

    (b) execute vasp

3. nscf projection, wavefunction from the DFT is projected unto spherical harmonics basis.

    (a) copy CHG CHGCAR WAVECAR from step 1

    (b) execute vasp for projection

    (c) execute wannier90

A.3 NEMO5

Regression test: `https://nanohub.org/tools/nemo/svn/trunk/NEMO/regression_test/numerical_tests/readin_wannier`

B. DATA LOCATION

All the simulation data, associated NEMO5 input decks used to generate figures in this thesis are provided with links in the Klimeck group SVN repository's version. **Click here for the link.** However, it is deleted in the Purdue library version due to formatting issue.